# Extraordinary bloom of toxin-producing phytoplankton enhanced by strong retention on the offshore Patagonian Shelf

Valeria Ana Guinder*[1], Urban Tillmann[2], Martin Rivarossa[3], Carola Ferronato[1], Fernando J. Ramírez[1], Bernd Krock[2], Haifeng Gu[4], Martin Saraceno[5,6,7]

[1] Instituto Argentino de Oceanografía (IADO), Consejo Nacional de Investigaciones Científicas y Técnicas (CONICET), Argentina. Universidad Nacional del Sur, UNS. Florida 4750, 8000 Bahía Blanca, Argentina.

[2] Alfred Wegener Institut-Helmholtz Zentrum für Polar- und Meeresforschung, Am Handelshafen 12, 27570 Bremerhaven, Germany.

[3] Instituto Nacional de Investigación y Desarrollo Pesquero, INIDEP, and CONICET. Paseo Victoria Ocampo, Escollera Norte 1, B7602HSA Mar del Plata, Argentina.

[4] Third Institute of Oceanography, Ministry of Natural Resources, Xiamen 361005, China.

[5] Centro de Investigaciones del Mar y de la Atmósfera (CIMA), CONICET, Facultad de Ciencias Exactas y Naturales, Universidad de Buenos Aires (UBA), C1063ACV, Buenos Aires, Argentina.

[6] Instituto Franco-Argentino de Estudio sobre el Clima y sus Impactos (IFAECI) CNRS-IRD-UBA-CONICET, Buenos Aires.

[7] Departamento de Ciencias del Océano y de la Atmósfera (DCAO), Facultad de Ciencias Exactas y Naturales, Universidad de Buenos Aires (UBA), C1063ACV, Buenos Aires, Argentina.

*Correspondence to: vguinder@iado-conicet.gob.ar

**Abstract:**

The extensive Patagonian continental shelf in the Atlantic Ocean is renowned for its high productivity associated with nutrient-rich waters that fertilise massive phytoplankton blooms, especially along the shelf-break frontal system. Growing evidence reflects this ecosystem as a hotspot for harmful algal blooms (HABs). Whether these HABs reach coastal areas or are exported to the adjacent ocean basin by energetic edge currents remains unexplored. During two oceanographic cruises in spring 2021, a bloom of dinoflagellates of the Amphidomataceae family was sampled over the outer shelf with a ten-day interval, at stations 40 km apart. The bloom was first sampled on November 16, with 32 million cells $L^{-1}$, and was still persistent on November 25, with 14 million cells $L^{-1}$. The magnitude of this bloom is a global record for this group so far reported in the literature. The toxin azaspiracid-2 (AZA-2) was detected in both stages of the bloom, with values up to 2122 pg $L^{-1}$. The most likely source of AZA-2 was *Azadinium spinosum* ribotype B. The bloom developed in vertically stable waters (60 m mixed layer depth) with elevated chlorophyll concentration. Water retention and the presence of fronts induced by horizontal stirring controlled the persistence and trajectory of the bloom in a localised area over the continental shelf, as evidenced by analysis of geostrophic surface currents, Lyapunov coefficients, and particle advection modelling. These findings underscore the importance of monitoring HABs in offshore environments, and the need to understand bio-physical interactions that govern bloom taxa assemblages and transport pathways.

## 1. Introduction

In marine environments, dinoflagellates are the primary toxin-producing group of protistan plankton and key causative agents of harmful algal blooms (HABs). As the most diverse group of toxic microorganisms, -e.g. *Alexandrium* spp., *Karenia* spp., *Dinophysis* spp., *Azadinium* spp., *Amphidoma* spp.-, dinoflagellates produce a wide range of toxins. Phycotoxins are natural intracellular metabolites synthesised by certain microalgae that can be transferred through the food web, having severe impacts on marine biota, ecosystems and human health (Anderson et al., 2015; Sunesen et al., 2021). Broadly, HABs were long thought to occur exclusively in coastal regions, due to their visible impacts on water quality and human-related activities, as documented for instance in the Argentine Patagonian Gulfs (Wilson et al., 2015; D'Agostino et al., 2019) and the Beagle Channel (Almandoz et al., 2019; Cadaillon et al., 2024). However, the perception of HABs as solely coastal events was biased, primarily due to greater monitoring efforts in coastal areas compared to the fewer studies conducted offshore (Hallegraeff et al., 2021; Sunesen et al., 2021; Anderson et al., 2021). In line with this trend, the expansion of the monitored area in the Argentine Sea from the coast to the outer continental shelf over recent decades has confirmed that toxic species are indeed common in offshore waters (Ramírez et al., 2022), especially associated with the shelf-break front (reviewed in Guinder et al., 2024). It is well known that dinoflagellates possess advantageous strategies for thriving in frontal systems, such as effective swimming, mucus and cyst formation, mixotrophy, and toxin production (Smayda, 2002; Glibert, 2016). However, the bio-physical mechanisms explaining the development of large harmful blooms on hydrographically complex shelves are still not fully understood mainly due to the lack of simultaneous taxonomic data and velocity fields at synoptic scales.

In oceanic waters, the permanence and spatial extent of discrete phytoplankton blooms are influenced by dispersal mechanisms that rely on diffusion and horizontal advection (Abraham et al., 2000; Mahadevan, 2016; Lehahn et al., 2017). Typically, the dispersion and stirring of phytoplankton blooms in the ocean have been studied using remote sensing of chlorophyll-*a* and models (Lehahn et al., 2007; Lévy et al., 2018; Ser-Giacomi et al., 2023), with few studies considering *in situ* sampling (Abraham et al., 2000; Giddings et al., 2014; Hernández-Carrasco et al., 2020) to assess the bio-physical couplings of bloom development and persistence. In addition to the considerable complexity of studying the dynamics of phytoplankton blooms in the ocean, which involve multiple physical (temperature, salinity, and mixing of water masses), biological (species competition, grazers), and chemical (nutrients) factors, monitoring HABs presents an even greater challenge (Pitcher et al., 2010; Wells et al., 2020; Iriarte et al., 2023). This includes the identification of the species involved in these blooms. It is precisely in this area where detailed studies, employing multiple approaches such as microscopy, molecular techniques, and toxin profiling (Smayda et al, 1997; Wells et al., 2020), make a significant contribution to understanding HABs' development and potential impacts.

The extensive Patagonian shelf-break front (35-55°S) in the SW Atlantic Ocean is a high productivity ecosystem, located ~200 to ~900 km offshore (Martinetto et al., 2019; Guinder et al., 2024). This permanent thermohaline front is associated with the upwelling of nutrient-rich waters of the westerly edge of the Malvinas Current, which fertilises the surface waters (Palma et al., 2008; Matano et al., 2010). Massive phytoplankton proliferations occur over the outer shelf in spring and summer (García et al., 2008; Carreto et al., 2016; Ferronato et al., 2023), including a variety of HAB-forming taxa and associated phycotoxins (Ramírez et al., 2022; Guinder et al., 2024). In fact, the increase in oceanographic studies focused on the detection of HABs along the outer Patagonian shelf has led to several new records of toxin-producing species and phycotoxins in the South Atlantic (Akselman et al., 2015; Guinder et al., 2018; Tillmann et al., 2019). The most conspicuous HABs are those formed by the nano-dinoflagellates of the Amphidomataceae family (Akselman and Negri, 2012; Fabro et al., 2019; Guinder et al., 2020; Tillmann et al., 2018; 2019), producers of the toxin azaspiracids (AZAs). These large HABs have emerged as important hazards in the productive Patagonian shelf-break frontal ecosystem, and include the four AZAs-producing species, i.e. *Azadinium dexteroporum*, *Az. poporum*, *Az. spinosum*, and *Amphidoma languida* (Krock et al. 2019). Amphidomataceans have been reported from different marine regions globally (Tillmann, 2018; Salas et al., 2021; Liu et al., 2023) but so far, the

maximum bloom abundances reported in the literature are from the Argentine Sea (Akselman and Negri, 2012). During the springs of 1991 and 1992, these dinoflagellates reached between 3 and 9 million cells per literre and caused water discoloration in the northern area (38-42°S; 58°-56°W) of the Patagonian shelf (Akselman and Negri, 2012). No toxin screening was performed at that time, but in spring 2015, an AZA-producing *Azadinium* strain was isolated from another large bloom in the area (Tillmann et al., 2019). Moreover, AZAs have been detected in the tissue of the scallop *Zygochlamys patagonica* since the early 90ies (Turner and Goya, 2015). These scallops form large seabed banks along the 100-meterre isobath between 38°S-48°S (Alemany et al., 2024), associated with the high phytoplankton productivity over the outer Patagonian shelf.

Despite the limited synoptic sampling in offshore waters, the prevalence of HABs in the Patagonian front highlights this ecosystem as a hotspot that requires further monitoring. The notably high abundance of Amphidomataceans over the outer shelf holds greater significance when assessing the potential risks that bloom dissemination may pose to both regional and global ecosystems. The evolution and transport of HABs remain poorly understood, as does the question of whether they may reach coastal areas or be exported offshore into the stirring Atlantic Ocean. The accumulation and dispersion of phytoplankton patches in complex shelf waters need to be addressed from an interdisciplinary perspective, combining remote sensing, modelling, and *in situ* sampling (Ferronato et al., 2025). In a recent study conducted on the outer Patagonian Shelf, the core of the Malvinas Current, and adjacent open ocean waters, we emphasized the key role of mesoscale energetic variability in modulating phytoplankton spring blooms (Ferronato et al., 2025). However, these observational studies combining multiple approaches at synoptic scale remain scarce in the region.

In this study, we characterised the bio-physical aspects of a large multispecific spring bloom of Amphidomataceans, detected through an unusual sampling effort that involved two research expeditions in November 2021. This HAB was observed at two sampling sites 40 km apart within a span of 10 days. We combined field observations of protistan plankton species composition and associated toxins, with remotely sensed ocean colour images of chlorophyll-*a* and geostrophic surface currents, particle tracking experiments, and Lyapunov coefficient analysis to assess the horizontal displacement and retention of the Amphidomataceae bloom within a mesoscale eddy. Furthermore, we aim to explore whether this HAB that developed in offshore shelf waters might reach coastal areas or be advected by the Malvinas Current, facilitating the dispersal of toxic species to other shelves and ocean basins.

## 2. Materials and Methods

### 2.1 Hydrography and productivity in the Patagonian continental shelf

Along the external margin of the Patagonian continental shelf, between 35°S and 55°S, a thermohaline front develops throughout the year, characterised by high biological productivity. The development of this front and the associated upwelling is due to the interaction of the energetic western boundary current system with the steep slope and the waters of the shelf, as well as the effect of winds and tides (reviewed in Piola et al., 2024). The Malvinas Current originates at ~55°S as a branch of the Antarctic Circumpolar Current **(Fig. 1)** and runs northwards at high velocity (mean surface velocities 45 cm/s, Piola et al., 2024) along the shelf break in two jets that meet at ~44°S (Frey et al., 2023). Then, at ~38°S, the Malvinas Current meets the warm and oligotrophic Brazil Current, which runs southwards, in the so-called Brazil-Malvinas Confluence, and waters are exported eastwards into the South Atlantic Ocean basin **(Fig. 1)**. In addition, another branch of the Antarctic Circumpolar Current gives origin to the Patagonian Current which runs northwards over the continental shelf, carrying diluted subantarctic waters **(Fig. 1).**

The interaction of the Malvinas Current with the irregular bottom topography generates upwelling of cold, nutrient-rich waters that fertilise phytoplankton over the shelf, together with the Patagonian Current (reviewed in Guinder et al., 2024). Phytoplankton blooms expand over the mid and outer shelf as reflected by a persistent satellite chlorophyll-*a* band, wider in

spring and narrower in summer along the shelf-beak front (Guinder et al., 2024). The magnitude of the upwelling has low seasonal variability and is heterogeneous along the extensive latitudinal range of the slope (Combes and Matano, 2018). Hence, productivity over the shelf varies spatially and temporally, and in consequence, multiple bioregions emerge, each characterised by unique phytoplankton phenological patterns, as revealed by climatological analysis of satellite-derived chlorophyll-$a$ (Delgado et al., 2023).

**2.2 Research cruises**

Two oceanographic expeditions were carried out during late-spring (November 2021) to study microbial plankton communities in the Argentine continental shelf and adjacent ocean basin (**Fig. 1**). The first research cruise, Ana María Gayoso (hereafter Gayoso, GA), took place aboard the R/V Bernardo Houssay (operated by PNA and CONICET, Argentina). This cruise was planned to analyse the pre-bloom conditions of the coccolithophore *Gephyrocapsa huxleyi* which blooms in early summer (December) on the Patagonian shelf. The location of the sampling stations was delineated tracking daily satellite-derived signals of chlorophyll-$a$ and particulate inorganic carbon (see Ferronato et al., 2025). Sampling occurred between November 16 and 22, 2021, at 10 stations distributed along the outer Patagonian shelf, the core of the Malvinas Current, and adjacent open-ocean waters (**Fig. 1**). The second cruise, Agujero Azul (AA), took place onboard the R/V Victor Angelescu (INIDEP and CONICET, Argentina). This multidisciplinary expedition was part of a national project aimed at assessing the pelagic and benthic biodiversity of this highly productive area known as the Agujero Azul (44-47°S; 62-57.5°W) (**Fig. 1**), with particular emphasis on commercially important species (Alemany et al., 2024). Sampling took place between November 25 and December 3, 2021, at 23 stations arranged along two cross-shelf transects in the Agujero Azul area (**Fig. 1**). We first provide a general overview of the *in situ* measurements (CTD) and water sampling conducted during both cruises for the analysis of plankton and nutrients. We then focus on the Amphidomataceae bloom observed over the shelf at station GA01 on November 16 and station AA09 on November 25, located approximately 40 km apart (**Fig. 1**).
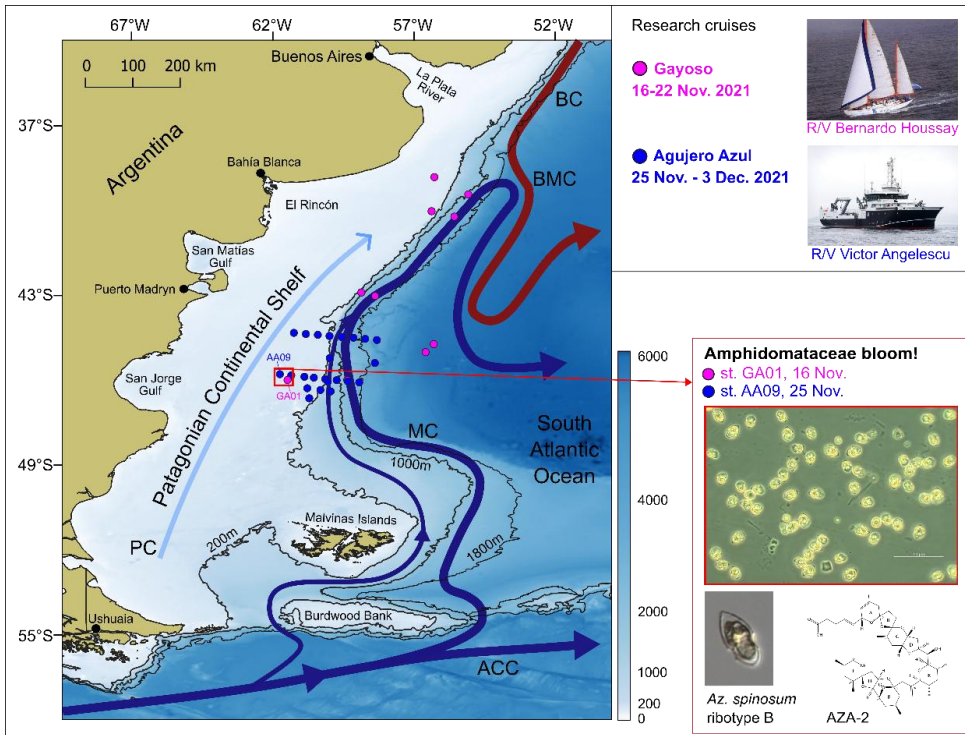
**Figure 1: Sampling stations of the research cruises Gayoso (pink dots, onboard R/V Houssay) and Agujero Azul (blue dots, onboard R/V Angelescu), and the main circulation pattern in the Argentine continental shelf and shelf break. The stations where the bloom of Amphidomataceae was observed are indicated with a red square: GA01 and AA09, sampled on November 16 and 25, respectively. Micrographs show the Amphidomatacean bloom and a cell of *Azadinium spinosum* ribotype B, producer of azaspiracid-2 (AZA-2). ACC: Antarctic Circumpolar Current, MC: Malvinas Current, BC: Brazil Current, BMC: Brazil-Malvinas Confluence and PC: Patagonian Current. Bathymetry from GEBCO, 2021. Isobaths of 200 m, 1000 m and 1800 m are displayed.**

**2.3  Remote sensing of surface Chl-*a* and  SST**

In order to contextualise the discrete observations of plankton within broader spatio-temporal dynamics, we explored satellite-derived surface chlorophyll-*a* concentration (Chl-*a* sat) data from the days of the cruises. In this sense, daily merged product with a 4 km resolution, provided by the GlobColour project (distributed by ACRI ST, France: https://hermes.acri.fr/), were downloaded. This ocean color product is generated from the fusion of the SeaWiFS, MERIS, MODIS-Aqua, and OLCI sensors and estimates the average Chl-*a* concentration in the surface layer (Maritorena et al., 2010). The fusion of data from different satellite sensors, combined with the quality control criteria used by GlobColour, enables enhanced spatial and temporal coverage. Eight-day temporal averages were calculated for the periods of November 12–19 and November 20–27, 2021. Additionally, daily Chl-*a* images were assessed from November 14 to 27 focused on the bloom area to track its short-term evolution. Due to high cloud covering, data is missing from November 22 to 24. To analyse Sea Surface Temperature (SST) during the sampling periods, daily NSST MODIS-Aqua level L3 images with a 4 km resolution were downloaded from https://oceancolor.gsfc.nasa.gov/. Eight-day temporal averages were also constructed for the periods of November 12–19 and

181  November 20–27, 2021. All images were processed using SeaDAS v8.3 and QGIS 3.38, mapped to the WGS84 reference
182  system (datum WGS84, ellipsoid WGS84), and restricted to the study area. The images were smoothed using a 'Non-Linear
183  Mean 3x3' filter.

185  **2.4** *In situ* **measurements and sample collection**

187  At each sampling station, continuous vertical profiles of temperature, salinity and fluorescence were measured. In Gayoso
188  cruise, a Sea-Bird 9 plus CTD and a fluorometer sensor Wet Labs FLRTD-5105 were used. In Agujero Azul cruise, a Seabird
189  SBE 9 Digiquartz CTD coupled with an ancillary Seapoint SCF chlorophyll fluorometer were used. To assess the vertical
190  stability of the water column, the Brunt-Väisäla buoyancy frequency (cyc h$^{-1}$) was computed using the function swN2 of the
191  package oce (Kelley et al. 2022) in R statistical software. Thereafter, the mixed layer depth (MLD, in meters) was defined at
192  the depth where the maximum value of the Brunt-Väisäla frequency was detected.
193  Niskin bottles attached to the CTD-rosette were used to collect water samples at the surface (5 m depth) for the analysis of
194  chlorophyll-*a,* dissolved inorganic macronutrients, protistan plankton by microscopy, genetic analysis of the species diversity,
195  and phycotoxins in field samples.
196  For chlorophyll-*a*, a volume of 400 mL was filtered through filter GF/F fiber-glass filters pre-combusted at 450 °C for 4 h. A
197  volume of 10 mL of 90 % acetone was used for pigment extraction during 24 hs (4 °C), and thereafter quantified using an
198  Agilent Cary 60 UV-Vis spectrophotometer. Concentration was estimated using the equations developed by Jeffrey and
199  Humphrey (1975).
200  For inorganic nutrients, the water samples filtered through Whatman GF/F fiber-glass filters pre-combusted at 450 °C for 4 h,
201  were stored at -20 °C in alkali-rinsed (NaOH, 0.1 M) polyethylene bottles. Nitrite, nitrate, ammonium, silicate and phosphate
202  were measured using a spectrophotometer Agilent Cary 60 UV-Vis following standard seawatermethods outlined by Hansen
203  and Koroleff (1999). These protocols for chlorophyll and nutrient determinations have been applied and intercalibrated for
204  other areas of the Patagonian Shelf (e.g. Ferronato et al., 2025; Gilabert et al., 2025).
205  Duplicate samples for plankton counts collected with Niskin bottles were preserved with Lugol (1% f/c) and formaldehyde
206  (1% f/c) in glass bottles (250 mL) and kept in dark and at 4 °C for their analyses under microscopy. Similarly, duplicate water
207  samples were collected by three vertical net tows (20 µm size pore) integrating the first 30 m depth for the identification of
208  protists' taxa.
209  For the quantification of azaspiracids (AZAs) as well as for genetic analysis of field species diversity, the same sampling
210  protocol was applied. A volume of 4-5 L of seawater from the Niskin bottles was pre-screened through a 20 µm mesh-size,
211  and subsequently filtered through 5 µm pore-size polycarbonate filters (Millipore, Eschborn, Germany) under gentle vacuum
212  (< 200 mbar). Filters were placed in 50 mL centrifuge tubes and preserved at -80 °C for further analyses in the laboratory.

214  **2.5  Plankton diversity analyses**

216  Morphological aspects of plankton cells were carefully observed under different light microscopes all equipped with
217  epifluorescence and differential interference contrast optics: a Nikon Eclipse E-400 microscope, a Zeiss Axioskop 2
218  microscope, and an inverted Axiovert 200 M. In order to measure length and width of cells, micrographs were taken at 1000
219  magnification under a Zeiss Axio Vert.A1 equipped with a digital camera AxioCam 208 Color, and under an Axioskop 2
220  equipped with a Axiovision digital camera. Thereafter, micrographs were processed with the software ZEN (v.2.7, Zeiss) and
221  Axiovision (v.4.8, Zeiss). Further, scanning electron microscopy (SEM, FEI Quanta FEG 200) was used to assess detailed
222  taxonomic features of the dinoflagellate species (e.g. arrangement of thecal plates, presence of pores and spines, etc). SEM
223  samples were treated following the protocol described in Tillmann et al. (2017). For the estimation of total protists' abundance

224    (in cells L$^{-1}$), seawater samples collected with Niskin bottles and fixed with Lugol were settled in sedimentation chambers and
225    single cells were counted under inverted microscope using a magnification of 400 following traditional techniques (Hasle,
226    1987). All protists larger than 5 µm in cell size were counted and classified into species or genera taxonomic levels, or merged
227    into taxonomic/functional groups organized in size ranges (e.g. ciliates between 10-20 µm, cryptophytes <10 µm,
228    *Gymnodinium*-type cell, Kareniaceae-type cell, etc.). In addition, to assess the relative abundance of the Amphidomataceae
229    species responsible for the multispecific bloom of this clade, subsamples (10-mL) were carefully counted with high taxa
230    resolution.

232    As an additional and complementary mean for analysing species diversity in the field samples, metarbarcoding was performed
233    specifically targeting the internal transcribed spacer (ITS1) region, following Liu et al. (2023). This information was used as
234    a complement to the exhaustive morphological taxonomy performed under light microscopy and SEM. In particular,
235    metabarcoding also allows the specific identification of ribotypes of Amphidomatacean species. For example, this is important
236    because for *Az. spinosum* different ribotypes have been shown to differ in toxin production and toxin profile (Tillmann et al.
237    2019). A detailed rationale for the Amphidomatacean species and ribotype designation is given in the Appendix B.

239    **2.6 Toxin identification and quantification**

241    Filters were repeatedly rinsed with 500 µL methanol until complete discoloration of the filters. The methanolic extracts were
242    transferred to a spin-filter (0.45 µm pore-size, Millipore) and centrifuged at 800 × g for 30 s, followed by transfer to
243    autosampler vials and stored at −20 °C until analysis. Toxin analyses were performed using high performance liquid
244    chromatography coupled to tandem mass spectrometry HPLC-MS/MS in the selected reaction monitoring (SRM) mode for
245    the detection of known AZA variants. In addition, precursor experiments of the ions *m/z* 348, 350, 360, 362, and 378 were
246    carried out to find potentially new AZA variants. Screened mass transitions and instrument parameters are detailed in Tillmann
247    et al. (2021).

249    **2.7 Lagrangian simulations and Finite Size Lyapunov Exponent analysis**

251    To explore the physical mechanisms that might explain the concentration of Aamphidomatacean measured in the two locations
252    sampled we used two complementary analysis: Lagrangian advection of virtual particles and Finite Size Lyapunov Exponents
253    (FSLEs).
254    The first technique consists on the analysis of trajectories of virtual neutrally buoyant particles that were obtained with an
255    algorithm that represents the advection process caused by surface currents. The advection equation:

$$X(t + \Delta t) = X(t) + \int_{t}^{t+\Delta t} v(x, \tau)\, d\tau \qquad (1)$$

259    where X is the three-dimensional position of a particle, $v(x, \tau)$ is the three-dimensional velocity field, is integrated using a
260    fourth-order Runge–Kutta scheme. Particles were released at the surface along 46°S and every 0.05 grades in the four regions
261    indicated in the **Appendix D**. The algorithm computes the particle positions based on initial location and knowledge of the
262    velocity field. A time step of one hour was considered. The accuracy of the trajectories obtained relies on the accuracy of the
263    velocity field used. For this experiment we considered geostrophic velocities obtained from satellite altimetry. In the northern
264    portion of the Argentine continental shelf, such surface velocities showed to be well correlated with *in situ* current
265    measurements (Lago et al., 2021). We therefore assume that the surface dynamics can be represented by satellite altimetry
266    derived data and use it as the input velocity field for the algorithm to advect the virtual particles. Geostrophic velocities derived

267 from gridded Absolute Dynamic Topography (ADT) of daily temporal resolution and ¼ of degree spatial resolution maps were
268 downloaded from CMEMS (https://marine.copernicus.eu/).

270 The second technique consists on the analysis of FSLEs images with a spatial resolution of 1/25° grid that were obtained from
271 AVISO (https://www.aviso.altimetry.fr). FSLEs ridges approximate the so-called Lagrangian Coherent structures which are
272 the generalization of stable hyperbolic trajectories of time independent flow. They are defined as the larger eigenvalues of the
273 Cauchy-Green strain tensor of the flow map. FSLEs are ~~strongly linked with~~defined by the exponential rate λ (d-1) of
274 separation of two neighbouring particles during a time advection t:

275 $$\lambda = t^{-1} \log(\delta f/\delta 0) \tag{2}$$

276 where δ0 and δf are the initial and final separation distance which are fixed before computation. FSLEs are commonly used as
277 an indicator of frontal activity and stirring intensity (d'Ovidio et al., 2004). Relatively large FSLEs values are associated with
278 formerly distant water masses, whose confluence creates a transport front (d'Ovidio et al., 2004; d'Ovidio et al., 2009). Fronts
279 identified as positive maxima (ridges) of FSLEs ~~have~~ exhibit a convergent dynamics transverse to them, ~~so that~~whereby passive
280 particles in their ~~neighbourhood~~ vicinity are attracted to the front and then advected along it (Della Penna et al., 2015).
281 Conversely, negative values of FSLEs indicate divergent dynamics, leading to the dispersion of particles away from the front.
282 In order to examine meso- and submesoscale frontal structures during phytoplankton blooms, daily FSLEs images from
283 November 10 to 25 were analysed. The daily images were used to create a video (**Appendix D**) to illustrate the daily evolution
284 of the FSLEs in the area where the phytoplankton bloom developed.

286 **3. Results**

288 **3.1 Satellite-derived chlorophyll-*a* during the sampling period**

290 During the Gayoso cruise (Nov. 12-19, **Fig. 2a**), a uniform, large band of high surface Chl-*a* concentration (between 4.0 and
291 32 mg m$^{-3}$) expanded over the mid and outer shelf. During the Agujero Azul cruise (Nov 20-27, **Fig. 2b**), the band of Chl-*a*
292 disaggregated and showed lower intensity (1.5 and 34 mg m$^{-3}$), but the Chl-*a* concentration was still high in the area of the
293 sampling stations **(Fig. 2b)**. The SST showed warming of the inner-mid shelf waters north of 44°S over the 8-day average
294 periods (around 14.5 °C in mid shelf) **(Fig. 2c, d),** but the SST remained yet constant at the sampling stations' area around 11
295 °C) (see **Fig. 4** and **Table 1**). The daily images of Chl-*a* from 14 to 25 November (**Fig. 3**) showed an abrupt proliferation of
296 phytoplankton on November 15 which notably intensified on November 16 when it reached the maximum concentrations
297 during the studied period (up to 35 mg m$^{-3}$). On this date, the extraordinary bloom of Amphidomataceae was sampled at GA01.
298 During the following days, the chlorophyll levels remained high in the area but became more disaggregated into variable
299 patches. On November 25, the sampling day at station AA09, Chl-*a* had decreased at station GA01 but remained intense in the
300 area **(Fig. 3)** with still extraordinary densities of Amphidomataceans at station AA09.

306
307
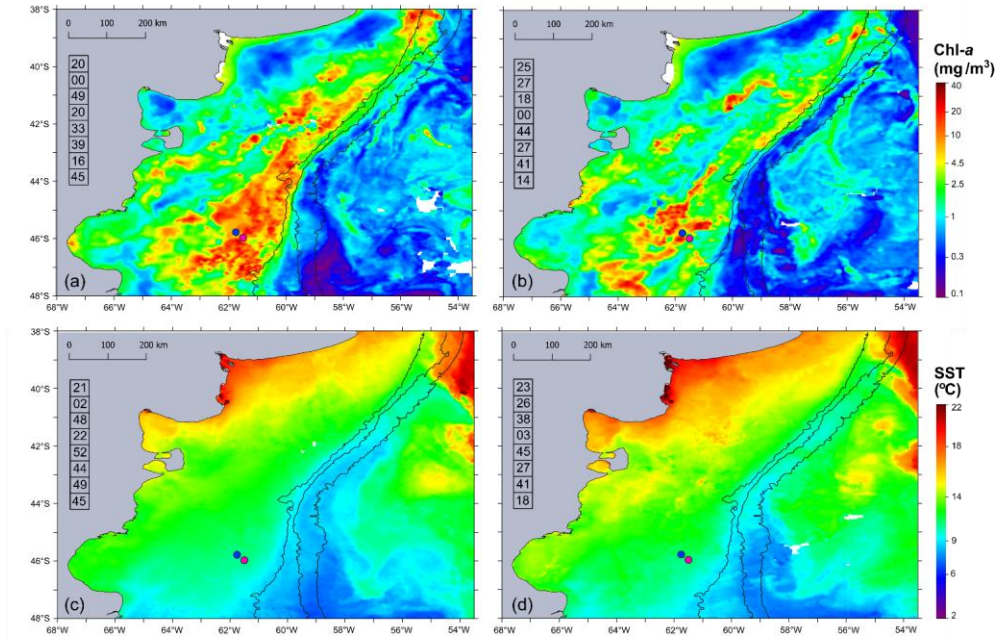
308 **Figure 2: Eight-day time mean of (a, b) satellite chlorophyll–*a* (Chl-*a* in mg m⁻³) and (c, d) sea surface temperature**
309 **(SST in °C) during the sampling period: (a) and (c) November 12-19, 2021, and (b) and (d) November 20-27, 2021.**
310 **From left to right, isobaths of 200 m, 1000 m and 1800 m are shown. The numbers in the column on the left side of each**
311 **panel correspond to the percentage of cloud-free pixels in each daily satellite image. The sampling stations GA01 (pink**
312 **dot) and AA09 (blue dot) are shown.**
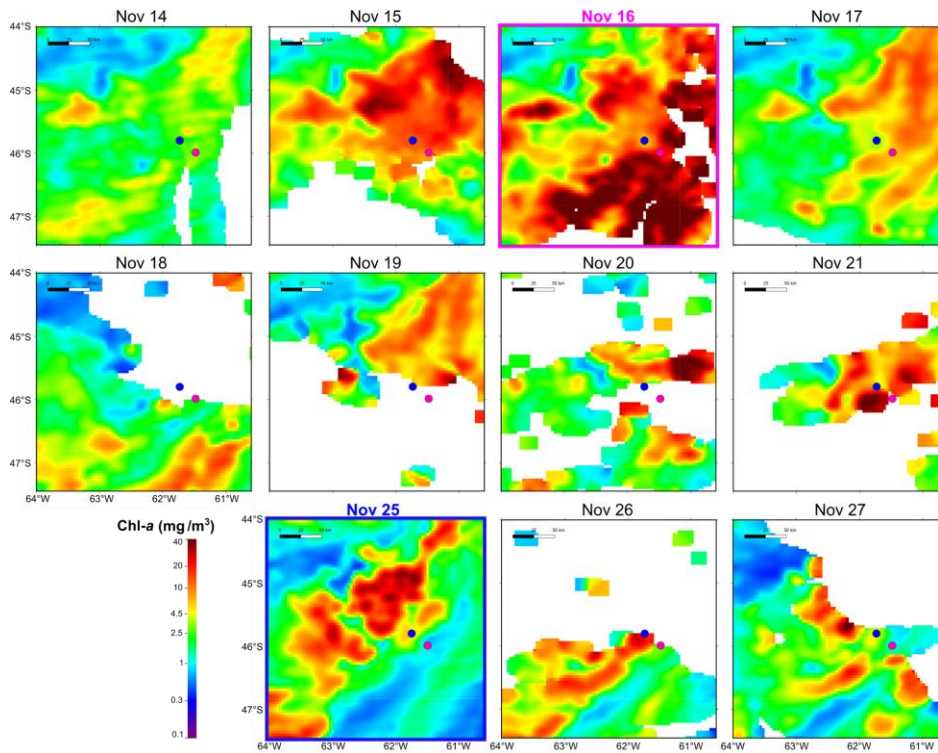
313
314
315 **Figure 3: Daily satellite-derived surface chlorophyll-*a* in the area of the sampling stations: GA01 (pink dot, sampled on**
316 **November 16, 2021), and AA09 (blue dot, sampled on November 25, 2021).**

317

318 **3.2 *In situ* biogeochemical properties and water column structure**

319

320 A reddish water discoloration was observed in the bloom area (45.5-46°S, 62-61°W) during the cruises. Surface water
321 temperature and salinity remained similar at both stations GA01 and AA09 sampled with a ten-day interval **(Fig. 4, Table 1)**.
322 Moreover, both stations displayed the same vertical structure in terms of temperature and salinity **(Fig. 4)**, the mixed layer
323 depth (MLD), and the subsurface chlorophyll maximum (SCM) **(Table 1)**. *In situ* chlorophyll-*a* concentration at the surface
324 was 20 µg L$^{-1}$ at GA01 and 4.5 µg L$^{-1}$ at AA09 **(Table 1)**. Dissolved inorganic macronutrients in surface waters were similar
325 in both stages of the bloom, except for nitrate and silicate, which were higher at AA09. In particular, the silicate recovered by
326 ~5 times towards the advanced stage of the bloom.

327

328
329
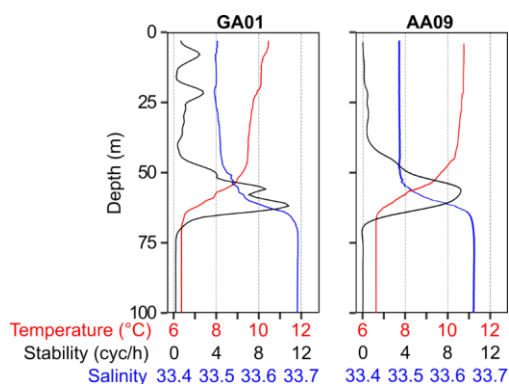
330 **Figure 4: Vertical profiles of temperature, salinity, and stability measured at the two blooming stations, GA01 (sampled**
331 **on Nov. 16) and AA09 (sampled on Nov. 25). Strong stratification is denoted by the water column stability (Brunt-**
332 **Väisäla buoyancy frequency) which indicates a mix layer depth (MLD) around 60 m.**

333

334 **Table 1: Surface values of physical and chemical variables measured at stations GA01 and AA09. Sea surface**
335 **temperature (SST), sea surface salinity (SSS), and concentration of *in situ* chlorophyll-*a* ~~(Chl-*a*)~~, and macronutrients.**
336 **The depth of the subsurface chlorophyll maxima (SCM) and the mix layer depth (MLD) is also displayed.**

Formatted Table

|  | GA01 | AA09 |
|---|---|---|
| Date | 16-Nov | 25-Nov |
| SST (°C) | 10.5 | 10.9 |
| SSS | 33.5 | 33.5 |
| SCM (m) | 15 | 10-25 |
| MLD (m) | 60 | 55 |
| Chlorophyll-a (-µg L$^{-1}$) | 20.0 | 4.5 |
| Nitrite (µM) | 0.48 | 0.33 |
| Nitrate (µM) | 1.77 | 3.57 |
| Ammonium (µM) | 1.32 | 1.32 |
| Silicate (µM) | 4.54 | 22.35 |
| Phosphate (µM) | 0.33 | 0.44 |

337
338

339 **3.3 Multispecificity of the Amphidomatacean bloom and azaspiracids**

340

341 Total protistan plankton of cell size larger than 5µm reached up 31.68 x10$^6$ cells L$^{-1}$ at station GA01, and 10-days later at
342 station AA09, the abundance was 13.69 x10$^6$ cells L$^{-1}$. Of all this total protist abundance, the Amphidomataceae clade
343 represented up to 99 % and 98 %, respectively **(Fig. 5)**, mostly dominated by the non-toxigenic species *Azadinium spinosum*
344 ribotype C and *Azadinium dalianense* **(Fig. 5 and 6)**, representing together >95 % of total Amphidomataceae **(Fig. 5)**.
345 Taxonomic identification up to species level was possible after exhaustive morphological examination of cells under light
346 microscopy **(Fig. 5)** and scanning electron microscopy **(Fig. 6)**. In the **Appendix A**, more micrographs of Amphidomataceans
347 are shown taken under light microscopy and scanning electron microscopy **(Figs. A01 to A10)**, along with the rationale for
348 the Amphidomatacean species designations. The ITS-based metabarcoding of species diversity detected in the field samples
349 at GA01 and AA09 are also shown in the **Appendix B**, which also support the dominance of *Azadinium spinosum* ribotype C

350 and *Az. dalianense*. In the detailed counting of protistan species in 10-mL subsamples, the well-recognized Amphidomataceae

351 species under inverted light microscopy for their individual quantification were: *Az. spinosum* ribotype B and ribotype C, *Az.*

352 *dalianense*, *Az. obesum,* and the smaller taxa *Az. dexteroporum*, *Amphidoma parvula* and *Am. languida* **(Fig. 5)**. This

353 distinction was based on morphological aspects combining the cell size and shape, such as the length/wide relation, and other

354 taxonomic aspects. For instance, a slender shape: *Az. spinosum* ribotype B; round: *Az. obesum*, short, tiny: *Az. dexteroporum,*

355 *Am. parvula* and *Am. languida*; with a bump in the hypotheca and a pyrenoid in the hyposome: *Az. dalianense*; with a spine in

356 the hypotheca: *Az. spinosum* ribotype C, *Az. dalianense*, and *Az. dexteroporum*. These and other taxonomic features were

357 further examined by SEM **(Fig. 6)**, for example the number and arrangement of the thecal plates, the presence of thecal pores,

358 etc. (see the **Appendix A**). Finally, other protists than Amphidomataceans **(Fig. 7)** contributed up to 1.0 and 2.2 % of the total

359 abundance at stations GA01 and AA09, respectively. Most of the other protists were heterotrophic and mixotrophic

360 dinoflagellates and ciliates. No diatoms were observed in the field samples. For an overview of the pure Amphidomataceae

361 bloom in the field samples (e.g. no mucus formation, no aggregates, cells undergoing cell division), low-magnification

362 micrographs obtained through light microscopy are presented in the **Appendix C**. The screen of all known and potentially

363 novel variants of azaspiracids, which are produced by Amphidomataceae, revealed the presence of solely azaspiracid-2 (AZA-

364 2) in both stages of the bloom, with field values of 2122 pg L$^{-1}$ at GA01 and 620 pg L$^{-1}$ at AA09.

365
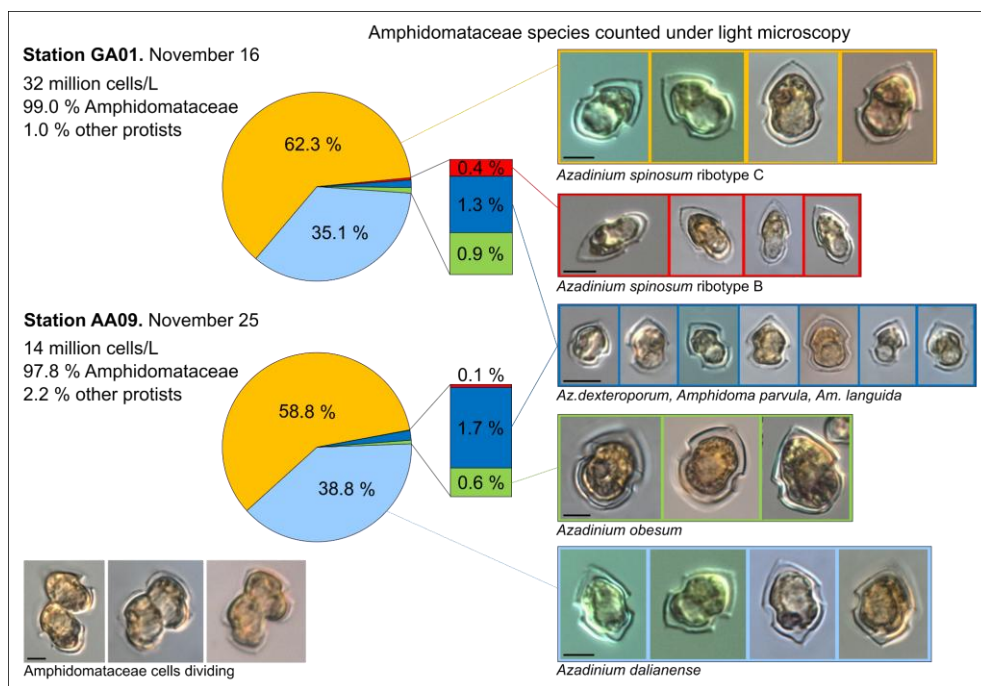
367 **Figure 5: Relative abundance (in %) of the Amphidomataceae species identified under light microscopy at stations**

368 **GA01 and AA09. The total abundance of protists at each station was 32 million cells L$^{-1}$ and 14 million cells L$^{-1}$,**

369 **respectively. From the total cells counted, Amphidomataceae represented up to the 99.0 % and 97.8 %, respectively.**

370 **The colours in the pie charts correspond to the same species at both stations. Scale bar: 5 μm.**
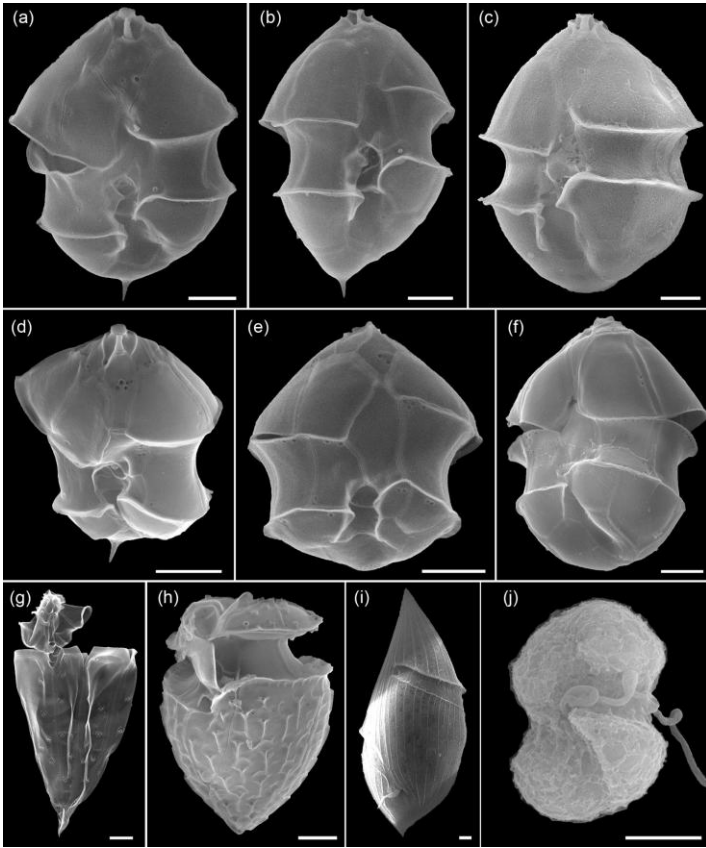
Figure 6: Scanning electron microscopy of Amphidomataeae species (a-f) and other dinoflagellates (g-j) at stations GA01 and AA09. (a) *Azadinium spinosum,* (b) *Az. dalianense*, (c) *Az. obesum*, (d) *Az. dexteroporum*, (e) *Amphidoma parvula*, (f) *Am. languida*, (g) *Oxytoxum gracile*, (h) *Oxytoxum laticeps*, (i) *Gyrodinium* sp., (j) unidentified gymnodinoid species. Scale bars = 2 μm. See the Appendix A for more micrographs of Amphidomataceans and for evidence and rationale for the Amphidomatacean species designations.
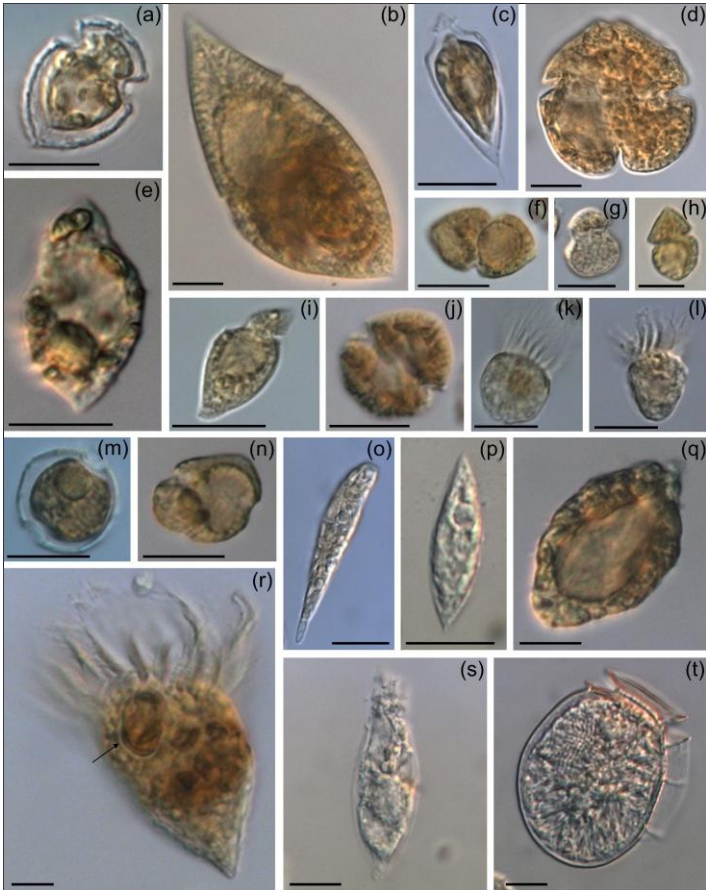
**Figure 7: Micrographs of other protists (1.0 - 2.2 % of total abundance) present in the bloom. (a)** *Oxytoxum laticeps*, **(b)** *Gyrodinium spiralis*, **(c)** *O. gracile*, **(d)** *Karenia* **sp., (e)** unidentified dinoflagellate, **(f)** *Gyrodinium sp.*, **(g, -h, j** **i)** unidentfied gymnodinoid cells, **(i)** *Katodinium* **sp., (k-l)** naked ciliates, **(m)** *Peridinella* **sp., (n)** Kareniacea-type cell, **(o)** Euglenophyte, **(p)** *Lessardia elongata*, **(q)** *Torodinium robustum*, **(r)** ciliate with an Amphidomataeae cell (arrow), **(s)** ciliate, **(t)** *Dinophysis* **sp. Scale bars = 10 µm, except in photos (g) and (h), scale bars = 5 µm.**

**3.4 Surface currents, particle advection model and description of the frontal systems**

The mean and standard deviation of the ADT during the sampling period (November 16 to 28, 2021) evidenced a mesoscale anticyclonic eddy of about 100 km in diameter in the area where the Amphidomataceae bloom was observed at the two sampling locations (**Fig. 8**). In addition, the modelled trajectory of the particles released along the zonal transect at 46°S on November 10 showed high retention at the blooming area over the continental shelf after running for 20 days (**Fig. 9**). On the contrary, high advection within the flow of the Malvinas Current was evidenced (**Fig. 9**). Notably, in the eddy area, particles slightly displaced southwards, remaining trapped in the area after 20 days since their release. The particles advected by geostrophic velocities suggest that the anticyclonic eddy acted as a potential mechanism to retain the Amphidomataceae bloom within the same location during the two synoptic samplings (**Fig. 9**). All the other particles released East and West of the eddy

396 displayed a different behaviour (**Fig. 9**), also shown in the **Appendix D** where four parcels of particles were advected from
397 November 16 to 25. West of the eddy they were advected northward at rather slow speed (average 5 cm/s) while East of the
398 eddy they increased their speed towards the north as they approached the continental slope. Within the core of the Malvinas
399 Current, speeds were as large as 0.8 m s$^{-1}$ (**Fig. 9**).
400
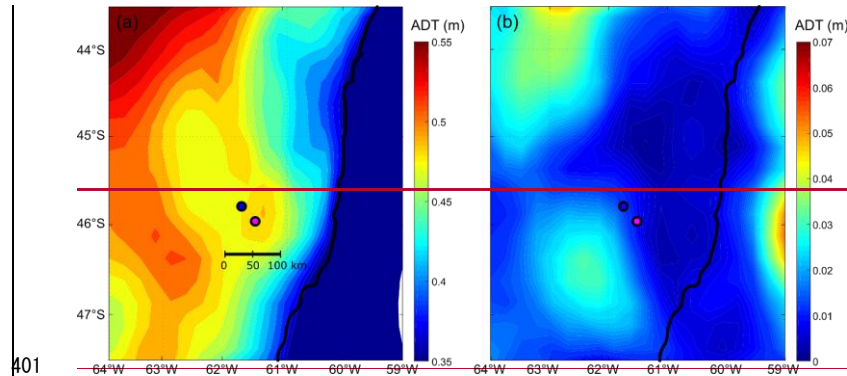
401
402
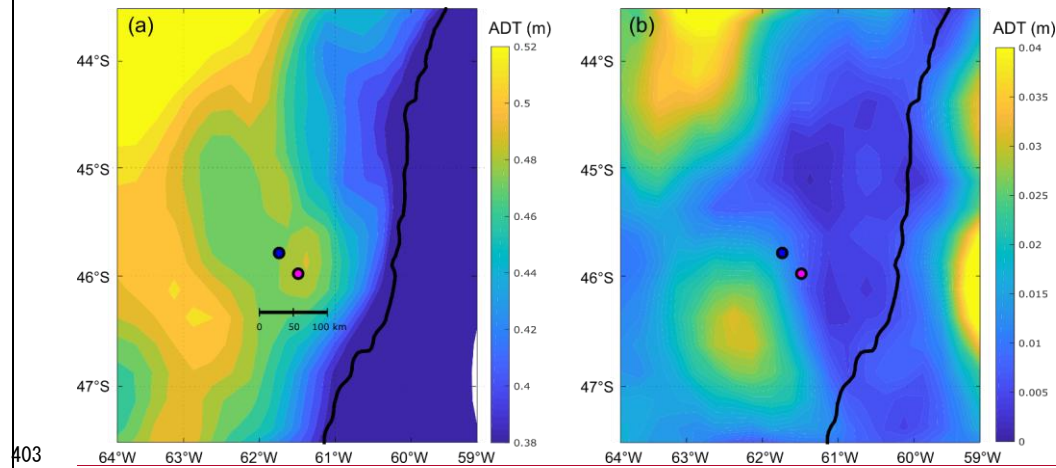
403
404 **Figure 8: (a) Mean and (b) standard deviation (std) of the Absolute Dynamic Topography (ADT, in meters) displayed**
405 **in colour scale, during the period November 16 to November 28, embracing the sampling period on both bloom stations:**
406 **GA01 (pink dot, Gayoso cruise) and AA09 (blue dot, Agujero Azul cruise).**
407
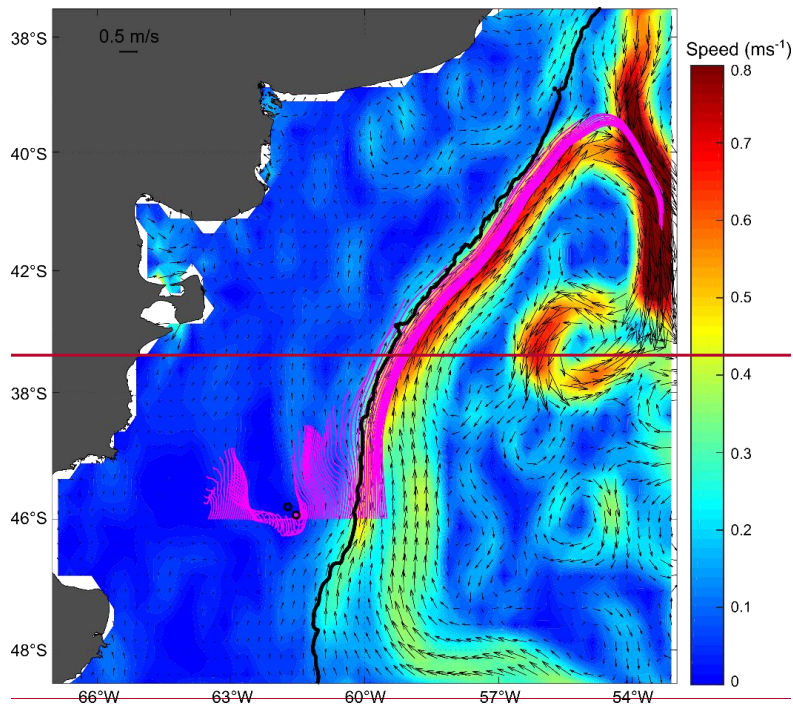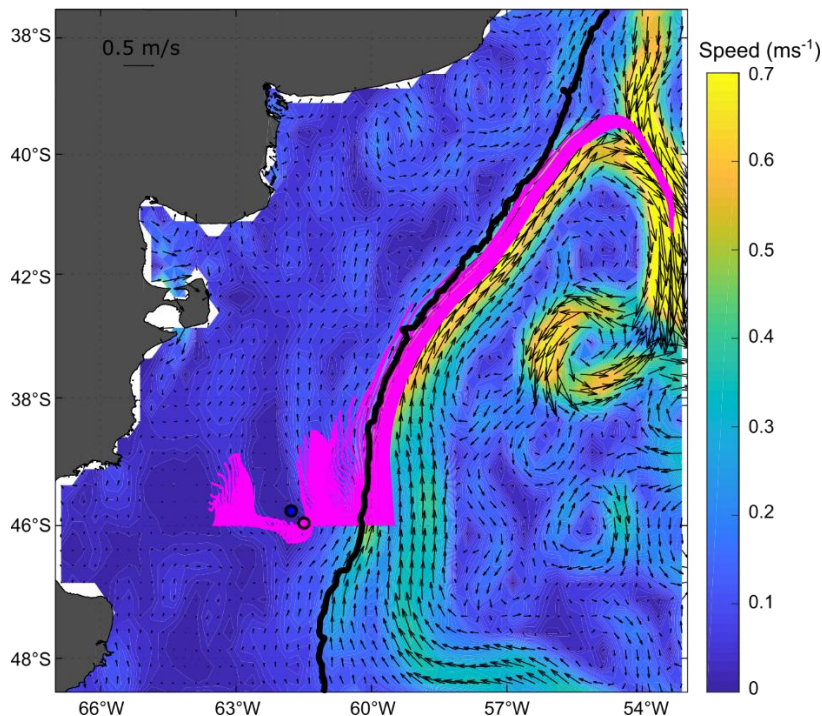
Figure 9: Particle advection after 20 days since particle release on November 10, 2021. Initial points: one particle every 0.05 grades along 46°S. Note the high retention and the distinct behaviour of particles in the area of the sampling stations: GA01 (pink dot) and AA09 (blue dot). Satellite altimetry geostrophic velocities averaged for the same 20 days are also displayed with black vectors; the magnitude of the averaged speeds is represented with colours in the background (m/s).

Moreover, the finite-size Lyapunov exponent (FSLE) ridges highlighted the stirring and hydrologically complex nature of the Southwestern Atlantic Ocean, associated with the high hydrographical heterogeneity of the oceanic waters (**Fig. 10**). Although FSLE were less intense over the shelf than in the adjacent oceanic waters, in the area where the Amphidomataceae bloom was sampled (pink dashed square in **Fig. 10**), two relatively strong FSLE ridges consistently kept both bloom stations within the same water mass during the period between the two synoptic samplings (**Fig. 11**).

422
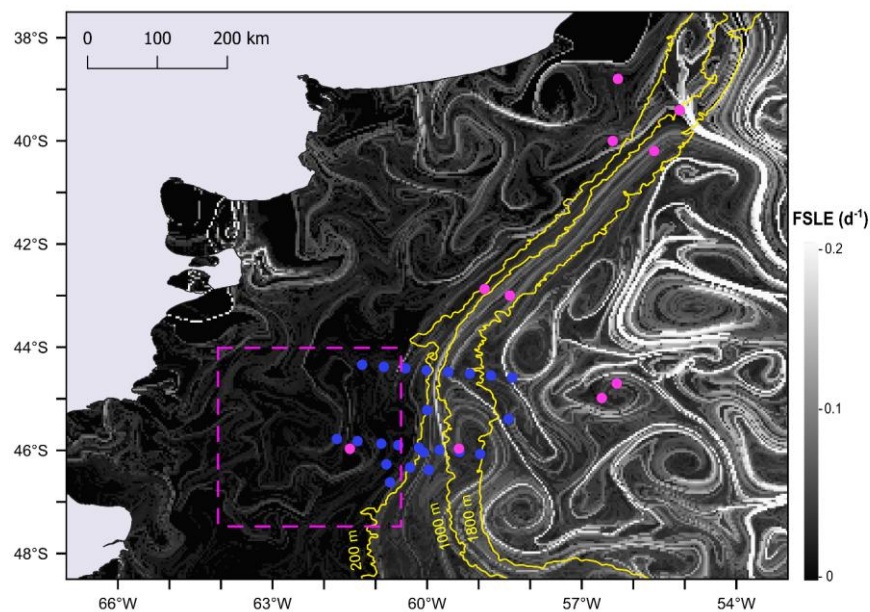
**Figure 10:** FSLE ridges computed ~~Fronts identified~~ as Finite-size Lyapunov Exponent (FSLE) ridges computed for November 16, shown against a grayscale background. All sampling stations from the Gayoso cruise (pink dots) and Agujero Azul cruise (blue dots) are indicated. November 16 corresponds to the sampling of the Amphidomataceae bloom at station GA01 (pink dot within the square marked by a dashed pink line). The square highlights the area shown in Fig. 11.

428
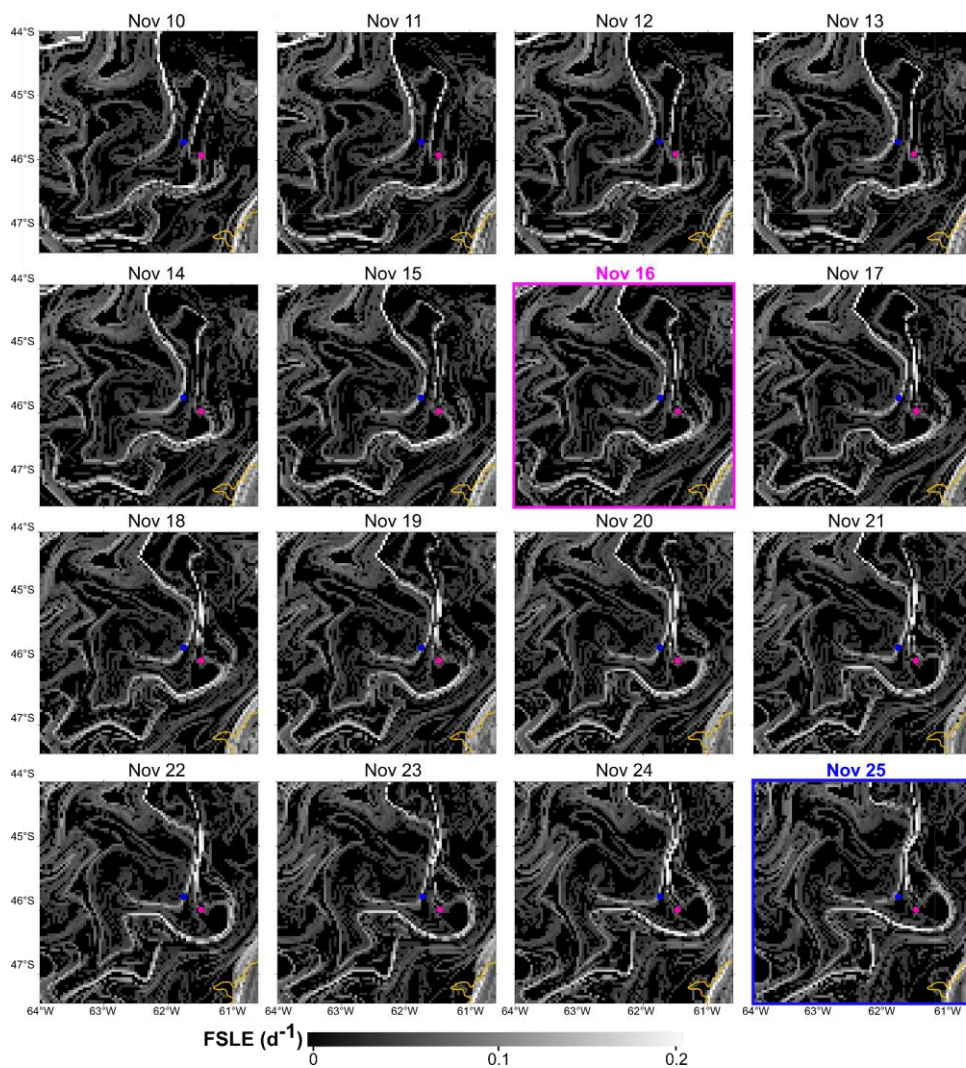
429
430
**Figure 11: Finite-size Lyapunov Exponent (FSLE) ridges in the area of the two locations with the Amphidomataceae bloom: GA01 (pink dot) sampled on November 16, and AA09 (blue dot) sampled on November 25. See the Video of these daily images in the Appendix D. The 200 m isobath is indicated in yellow.**

### 4. Discussion

This study is unique from both biological and physical perspectives due to the following factors: (i) the Amphidomataceae bloom observed in spring 2021 in the Argentine Sea, with up to 32 million cells per lit~erre~, represents the largest bloom of this clade ever recorded globally; (ii) unusual sampling in offshore shelf waters with two vessels over a ten-day interval allowed for synoptic observations of the bloom at two active developmental stages; (iii) simultaneous ecological characterization of

the bloom and surface currents and fronts provided insights into patch stirring and the short-term evolution of the bloom; (iv) field quantitative abundance data for Amphidomataceae are rare, and to our knowledge, this is the first detailed description of species abundance in field samples, combining light microscopy, electron microscopy, and metabarcoding; (v) the relatively low abundance of *Azadinium spinosum* Ribotype B indicated high AZA-2 cell quotas; (vi) the fine-taxon assessment of the Amphidomataceae bloom revealed biogeographical patterns and strain-specific toxic potential; and (vii) the use of interdisciplinary approaches sheds light on the bio-physical coupling underlying the persistence and horizontal transport of this extraordinary bloom in offshore shelf waters.

### 4.1. Amphidomataceae blooms over the Patagonian shelf

The phytoplankton spring and summer blooms in the Patagonian shelf display a southward progression related to the seasonal thermal cycle. In early spring (September-October), the water column stratifies north of ~45°S, favouring the proliferation of opportunistic micro-diatoms in the nutrient-rich, well-lit surface layers (Ferronato et al., 2023). South of ~45°S, the bloom initiates later in spring-early summer (December-January) and continues until autumn (March) (revised in Guinder et al., 2024). The distribution of surface Chl-*a* during the time of the cruises was indeed indicative of mid-late spring phytoplankton bloom over the Patagonian shelf, following the thermal stratification. Here, blooms of nanoflagellates and dinoflagellates are triggered by combined vertical stability and nutrient-depleted surface waters (especially silicates) after the early-spring blooms of large diatoms (Balch et al., 2014; Carreto et al., 2016). During the Gayoso cruise, detailed analyses of plankton communities and microbial carbon fluxes at all sampling stations revealed a latitudinal shift from more heterotrophic to more phototrophic activity toward the south (Ferronato et al., 2025; Gilabert et al., 2025). The massive proliferation of Amphidomataceans in mid-November 2021 was in line with this successional pattern. These nano-dinoflagellates bloomed in a stratified water mass with a deep mixed layer depth (~60 m). While dinoflagellates are less effective at nutrient resorption compared to diatoms, they can move throughout the stable water column to find light and nutrients (Glibert, 2016), especially at low phosphate levels (Lin et al., 2016) as observed at the stations GA01 and AA09 with high nitrate-to-phosphate ratios.

The success of the multispecific bloom of Amphidomataceae may be attributed to a combination of multiple intrinsic and extrinsic factors. For instance, their small cell-size, unique swimming modes and the production of azaspiracids may have alleviated grazing pressure (Tillmann et al., 2019). In fact, in the fixed samples, it was observed that many cells were obviously active and undergoing cell division and that these nanoflagellates were overwhelmingly the predominant photosynthetic protists responsible for the high Cehl-*a* levels, with negligible abundance of micro-grazers accompanying the bloom development. The presence of less than 2% of other protists (mixotrophs and heterotrophs) could be also related to a delay in the recovery of predators following the early blooms of microdiatoms, as well as to an abrupt development of the Amphidomataceae bloom, which may have prevented micrograzers from taking advantage of the available food. Another observation supporting the active persistence of the bloom was the pristine condition of the microenvironment surrounding the dense populations of Amphidomataceae (see **Appendix C**), with no aggregates or mucus formation typically observed in the late stages of blooms (Genitsaris et al., 2021). Furthermore, no competitors for light and nutrients were detected in the samples; specifically, no diatoms were found during microscopic examination. This may explain the rapid recovery of silicates (from 5 to 22 µM) over the 10-day persistence of the Amphidomataceae bloom, as these silicates were not being utilised by silicate-requiring species. A similar observation was noticed during a bloom induced by iron-fertilization in the Southern Ocean, where diatoms predominated and silicate levels decreased from 10 to 6 µM within the bloom patch over the course of 12-days (Abraham et al., 2000).

### 4.2. Highest abundance ever recorded for a bloom of Amphidomataceans

With 17 described species of *Azadinium* and 14 of *Amphidoma*, the Amphidomataceae represent a small but diverse group of dinoflagellates. Most of these species are very similar in size and shape, which makes the qualitative identification and, in particular, the species specific quantification in field samples difficult. Hence, characterising the cryptic species of the multispecific bloom of Amphidomataceae in this study represented a major challenge, where a reliable species identification was achieved by the combination of several diagnostic details using electron microscopy. Light microscopic counting of fixed samples provided high quantitative accuracy, but reliable species identification was only possible in a few cases. Complementing the identification by microscopy with metabarcoding specifically targeting the internal transcribed spacer (ITS1) region (Liu et al., 2023), allowed for the detailed characterization of Amphidomatacean species diversity in the field samples. By combining the three approaches we were able to identify ribotypes and the toxic species, including previously described Amphidomataceae species for the Argentine Sea (Fabro et al. 2019; Tillmann et al., 2019; 2021) or species still undescribed in the global seas (see the **Appendix A**).

In the North Atlantic, AZA-1 (and its producing species, *Az. spinosum* ribotype A), has been identified as one of the most prevalent toxins among a wide range of AZA variants (Tillmann et al. 2021). Bloom density of Amphidomataceae around Ireland have been reported as $8.3 \times 10^4$ cells L-1 for *Az. spinosum* (Wietkamp et al. 2020) and $47 \times 10^5$ cells $L^{-1}$ for *Amphidoma languida* (McGirr et al. 2022) and a small bloom of *Am. languida* in the North Sea with $1.2 \cdot 10^5$ cells $L^{-1}$ has also been described (Wietkamp et al. 2020). In this region, cases of human intoxication with azaspiracids have been linked to the consumption of contaminated mussels from the Irish West coast, where blooms in the shelf-break area can reach coastal shellfish beds through wind-driven advection (Raine, 2014). Notably, in the Argentine Sea, only AZA-2 has been detected in field and culture samples (Turner and Goya, 2015; Fabro et al., 2019; Tillmann et al., 2019; Guinder et al., 2020), and so far, no poisoning events have been attributed to AZAs.

In this study, relatively high levels of solely AZA-2 were detected in bloom samples. A toxin profile of solely AZA-2 is up to now only known for the Argentine strain H-1-D11 of *Azadinium spinosum* ribotype B (Tillmann et al., 2019), and this ribotype was also identified in the present bloom. Relating AZA quantities to the relatively low abundance (0.1 to 0.4 % of total Amphidomataceae) of *Az. spinosum* ribotype B revealed AZA-2 cell quotas of 17-42 fg per cell, which is an order of magnitude higher that the cells quota of 2 to 9 fg per cell for strain H-1-D11 grown under laboratory conditions (Tillmann et al. 2019). In fact, *Az. spinosum* of ribotype A producing AZA-1 and -2 is the primary causative agent of AZA poisoning in Europe (Tillmann, 2018). However, the large majority of cells of *Az. spinosum* in the present bloom sample is from ribotype C, which is, based on analyses of several strains from Argentina, non-toxigenic (Tillmann et al 2019), and all globally available strains (including strains from Argentina) of the other co-dominant species in the bloom, *Az. dalianense*, (Tillmann et al., 2019), also do not produce azaspiraids. In the Chilean continental shelf in the SE Pacific, AZAs have been detected in scallops and mussels (López-Rivera et al., 2010), but no intoxication events or large blooms of this clade have been documented (Iriarte et al., 2023). Other *Azadinium* cells have been observed widely distributed in inner seas along the coast of Chile, but with no further characterization of their potential toxicity (Iriarte et al., 2023; Corredor-Acosta et al., 2025). Only *Az. poporum* has been described as an AZA producer in Chilean waters (Tillmann et al., 2017a). Likewise in Peru, a relatively high bloom (up to one million cells per liter) of *Az. polongum* was detected in the summer of 2014, with no AZA production (Tillmann et al., 2017b). Although the continental shelves of Chile-Perú and Argentina have different hydrology, both span similar latitudinal gradients along the South American coasts and are influenced by the Humboldt and Malvinas Currents, which share a common origin in the Circumpolar Antarctic Current. Strikingly, both shelves exhibit different populations of Amphidomataceae, despite the expectation that ocean currents could serve as transport pathways for HAB species, promoting their dispersion (Giddings et al., 2014). This suggests that additional factors, such as coastline configuration and bottom topography, play a role in water mixing and retention processes, and ultimately the development of HABs (Pitcher et al., 2010).

**4.3. Spatio-temporal evolution of the bloom: retention and stirring**

527

Phytoplankton bloom initiation, magnitude, and persistence rely on a host of biogeochemical and physical processes. As discussed in previous sections, the explosive onset of the bloom of multiple species of Amphidomataceae was associated with a combination of water column stability, the negligible presence of micrograzers, and the ecological traits of this group that facilitate massive proliferation. However, these conditions alone do not fully explain the persistence of this bloom, which was sampled 10 days later at a location 40 km away in the offshore waters of the Patagonian shelf, where strong surface currents were expected to disperse plankton blooms. The persistence of this extraordinary bloom, characterized by its remarkable magnitude and consistent species composition, indicates the retention and accumulation of the bloom patch within the same water mass. In addition to the biological evidence confirming the presence of the same Amphidomataceae bloom at both sampling stages, analyses of circulation through satellite altimetry showed that an anticyclone of about 100 km of in diameter was the key feature responsible for the responsible feature to retaining the bloom within the two sampling stations. The retention that the eddy caused was evidenced by two Lagrangian experiments. In the first one, the trajectories of virtual particles released within the eddy show that almost none of the particles escaped from the eddy during the 10 days that separated the two sampling stations. In the second one, FSLEs maps showed that no mesoscale fronts separated the two sampling stations during those days. Both stations remained within the same water mass delimitated by two FSLEs with negative values, which indicate divergence of plankton transverse to the filaments, enhancing the retention of the bloom. Two potential scenarios could explain this: (1) the same patch remained in the area over the ten days of sampling, occupying an area of 40 km or larger (**Fig. 12a and b**), or (2) a smaller bloom patch was initially detected at station GA01 and then transported by stirring towards AA09 (**Fig. 12c**). Sampling with higher spatial and temporal resolution of bloom initiation, development, species succession, and collapse would have been necessary to distinguish between scenarios (1) and (2).  A less likely scenario is that (3) two Amphidomataceae blooms developed independently at both locations (**Fig. 12d**). This situation scenario is improbable due togiven the complex interplay of physical and biological interactions processes that drive govern bloom development. On the physical side, advection, accumulation, and stirring of water masses act as selective forces , such as variable stirring (Abraham et al., 2000; Lehan et al., 2007; Della Penna et al., 2015) favoring the proliferation of certain species or functional groups over others, depending on local and transient conditions and changing environmental conditions that select for different species and functional groups across diverse spatio-temporal scales ( Levy et al., 2018; Hernández-Carrasco et al., 2020; Mangolte et al., 2023). Biologically, additional layers of variability—including interspecific competition, grazing pressure, successional dynamics, toxin production, and cyst formation—further shape bloom composition and trajectory. Considering the influence of such dynamic and site-specific factors, the independent development of blooms with identical species composition and relative abundances at two separate locations is unlikely. Furthermore, no dormant cysts of Amphidomataceae have been reported, ruling out the possibility of localized population outbreaks from a resting stage, as has been observed for other dinoflagellates forming HABs in frontal systems Moreover, no dormant cysts of Amphidomataceae are known, which could explain population outbreaks in specific locations, as observed in frontal areas for other dinoflagellates forming HABs (Smayda, 2002; Akselman et al., 2015).

561

562
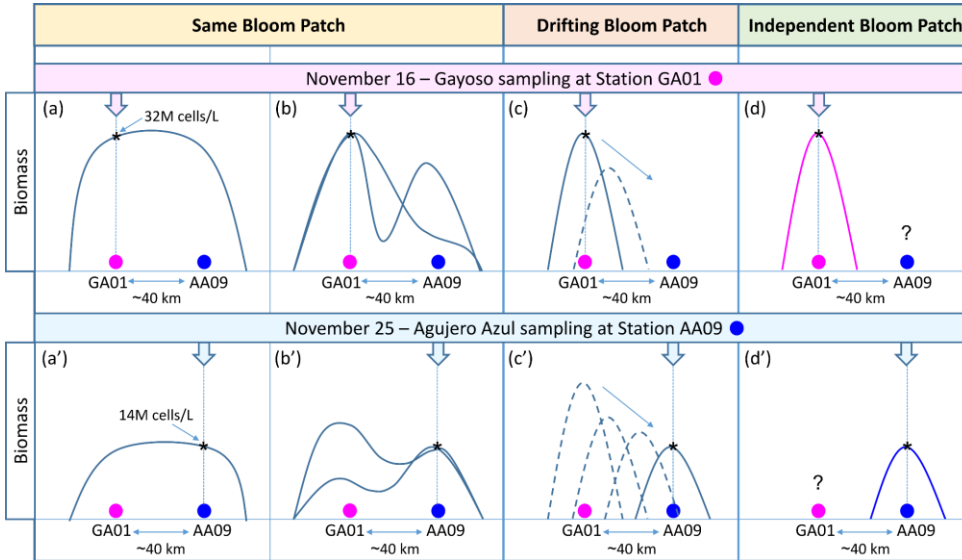
563 **Figure 12: Hypothetical scenarios of the spatio-temporal evolution of the Amphidomataceae bloom during the 10-day**

564 **period between the synoptic sampling at the two stations 40 km apart: GA01 (pink circle) and AA09 (blue circle). The**

565 **bloom's biomass was 32 million cells L$^{-1}$ at GA01 and 14 million cells L$^{-1}$ at AA09. In the Same Bloom Patch (a-a' and**

566 **b-b'), the bloom covered an area encompassing both sampling stations. The bloom developed such that the biomass**

567 **was either distributed homogeneously across the patch (a-a') or heterogeneously (b-b'), resulting in variable biomass**

568 **patterns over time and space. In the Drifting Bloom Patch (c-c'), the water mass with the Amphidomataceae bloom**

569 **detected at station GA01 was transported by currents towards station AA09, where the bloom was detected with lower**

570 **biomass but still with high intensity. The Independent Bloom Patch (d-d') suggests that two discrete, autonomous**

571 **Amphidomatacean blooms developed locally at each sampling station.**

572

573 Additionally, the hydrographically complex Southwestern Atlantic creates a variety of microhabitats at the meso- and

574 submesoscale. These include areas of upwelling, downwelling, eddies, retention, and dispersion (Becker et al., 2023; Beron-

575 Vera et al., 2020; Salyuk et al., 2022; Saraceno et al., 2024). This spatial heterogeneity enhances the development of variable

576 nutrient patches and phytoplankton productivity (Lehahan et al., 2017; Levy et al., 2018; Hernández-Carrasco et al., 2020;

577 Ser-Giacomi et al., 2023). During the Gayoso cruise, contrasting phytoplankton assemblages and bloom types were observed

578 at all sampling locations, including distinct blooms of dinoflagellates, coccolithophores, diatoms, and nanoflagellates. These

579 variations were related to substantial heterogeneity in surface velocities and environmental conditions across the region

580 (Ferronato et al., 2025). It is important to highlight that the bloom of Amphidomataceae at GA01 and AA09 was not observed

581 at any other station during the Agujero Azul cruise. In the Gayoso cruise, this clade was only observed in relatively high

582 abundance at GA10, located in the northern area over the shelf, where species assemblages were significantly different

583 (Ferronato et al., 2025). In this study, while the estimation of the retention of the Amphidomataceae bloom is certainly limited

584 by the accuracy of satellite altimetry maps, the documented 100 km diameter of the eddy is a reasonable size that can be

585 distinguished using the gridded satellite altimetry maps produced by CMEMS. Although this retention is transient, this

586 particular circulation facilitated the massive development of the Amphidomataceae bloom, with no evidence that this patch

587 was advected to the Malvinas Current, as observed with drifters released east of the bloom area in spring 2021 (Saraceno et

588 al., 2024). Our results highlight the importance of studying the evolution of toxic phytoplankton blooms on continental shelves,

589 focusing on the bio-physical coupling that drives their patchy nature, persistence, and transport, in order to capture short-lived
590 blooms and their potential to cause toxic outbreaks.
591
592 **5. Conclusions:**
593
594 We present an example where mesoscale (100 km) circulation on the Patagonian Shelf acted as ~~the~~ a crucial physical
595 driver that prevented the dispersion of an Amphidomatacean bloom. As a result, the bloom persisted for 10 days in the
596 same area. While our study provides valuable insights, it has limitations, as it only explores physical processes at a
597 mesoscale resolution, whereas sub-mesoscale processes are crucial for understanding divergence, convergence, and the
598 mixing of plankton and nutrients within and between water masses. We also note that the collection of samples from
599 only two synoptic stations, along with the incidental detection of the Amphidomatacean bloom during two cruises with
600 different ecological objectives, limited our ability to track the detailed spatial and temporal evolution of the bloom. One
601 strategy to overcome these limitations would be continuous sampling of the bloom, which could be achieved through a
602 Lagrangian experiment. In this approach, water samples would be collected following drifters that track surface currents.
603 At the same time, detailed biodiversity analyses of the bloom should be conducted, including the succession of species
604 and functional groups in relation to their differential uptake of nutrients, grazing pressure, and the potential exchange of
605 plankton and nutrients between neighboring water masses.
606
607
608 **Appendix A**
609
610 **A1. Estimation and categorization of Amphidomatacean species diversity**
611 For the present study, we combined light microscopy (LM) quantification, scanning electron microscopy (SEM) examination,
612 and metabarcoding to characterize the field samples as accurately as possible, both qualitatively and quantitatively. Generally,
613 the following species of Amphidomataceae were identified:
614
615 **A1.1. *Azadinium spinosum***
616 Specimens were identified with SEM as *Az. spinosum* based on the combination of (1) presence of an antapical spine, and (2)
617 presence of a ventral pore located on the right side of the suture of Plate 1' and 1" (Fig. A01). The vast majority of cells thus
618 identified as *Az. spinosum* had a somewhat broader cell shape. Generally, identification of *Az. spinosum* is complicated as there
619 are several different ribotypes (Tillmann et al., 2021), which notably differ in azaspiracid toxin presence and profile. In a
620 previous study from the Argentine shelf region, it was shown that 23 out of 24 isolated strains of *Az. spinosum* were assigned
621 to the non-toxigenic ribotype group C, and cells from these strains also had a somewhat broader cell shape (Tillmann et al.,
622 2019). Metabarcoding of the present bloom sample revealed that the most common sequences showed a high match with
623 sequences of these Argentine ribotype C strains. A dominance of non-AZA-producing *Az spinosum* (ribotype C) also aligns
624 with the finding that no AZA-1, the marker toxin of the toxigenic *Azadinium spinosum* ribotype A strains (Tillmann et al.,
625 2021), was detected in the field samples. In the quantitative light microscopy (LM) counts, all medium-sized cells (length >
626 12 µm) with a rounded hypotheca and an antapical spine were thus categorized as *Azadinium spinosum* ribotype C.
627

628
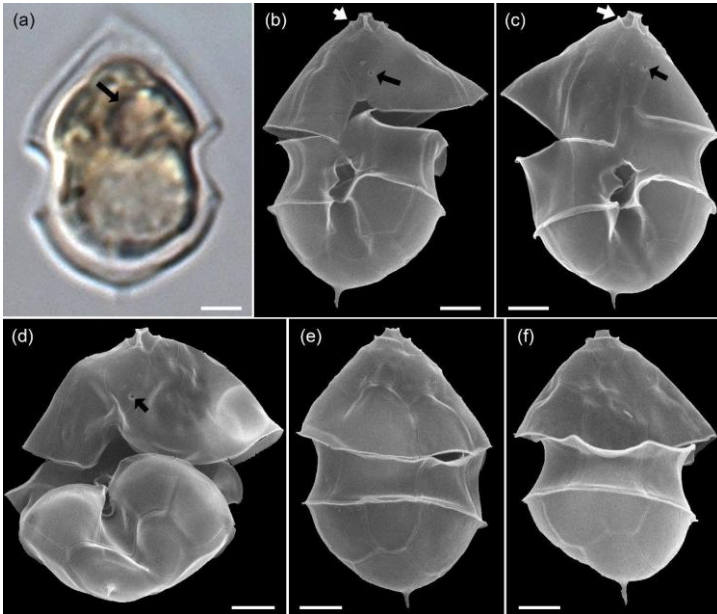
629 **Figure A01: LM (a) and SEM (b-f) of cells of the Amphidomatacean bloom stations identified as *Azadinium spinosum***
630 **ribotype C. (b–d) Cells in ventral view. (e, f) Cells in dorsal view. Note the pryrenoid (black arrow in a), the position of**
631 **the ventral pore (black arrows in b, c, d), the rim around the pore plate (white arrows in b, c) and the distinct antapical**
632 **spine. Scale bars = 2 μm.**

633

634 Recent studies have revealed the presence of a new, molecularly distinct species of *Azadinium* in the North Atlantic, which is
635 morphologically indistinguishable from *Az spinosum* and is currently provisionally referred to as *Azadinium* cf. *spinosum*
636 (Tillmann et al., 2021). Therefore, it cannot be ruled out that this species was also present in the samples, but metabarcoding
637 showed no evidence of the presence of *Az.* cf. *spinosum* in the bloom samples.
638 In addition to these broader cells of *Az. spinosum* ribotye C cells, LM analysis revealed a (much rarer) presence of distinctly
639 slender cells with an antapical spine (Fig. A02a). Such cells perfectly correspond to cell shape of a single strain H-1-D11 from
640 Argentina identified as a ribotype B strain of *Az spinosum* (Tillmann et al., 2019), and this strain is depicted here for comparison
641 (Fig. A02c, d). In SEM, specimen of slender shape lacked the rim around the pore plate (Fig. A02b), which is the morphological
642 diagnostic feature differing in ribotype B strains from ribotype A and C strains, which all have a thick rim. Additionally,
643 metabarcoding showed conformity of some sequences with other ribotype B *Az. spinsum* strains (e.g. 99% similarity with the
644 Argentinean strain H-1-D11). Consequently, all slender cells with an antapical spine quantified in LM were categorized here
645 as *Az. spinosum* ribotype B. Strain H-1-D11 from Argentina was shown to produce solely AZA-2 (Tillmann et al., 2019). As
646 this was the only AZA detected in our field sample, this is additional support for this *Az. spinosum* ribotype B designation.
647

648
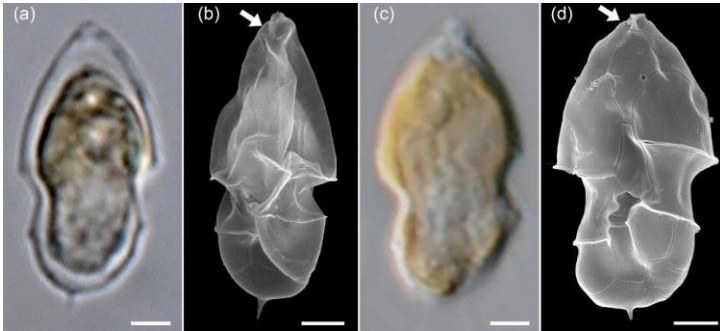
649 **Figure A02: LM (a), and SEM (b) of cells of the ~~A~~amphidomatacean bloom stations identified as *Azadinium spinosum*.**

650 **For comparison, LM (c) and SEM (d) of cells of strain H1-D11 of *Azadinum spinosum* ribotype B isolated from the**

651 **Argentine shelf in 2015. Note the elongated cells shape, the distinct antapical spine, and the lack of a rim around the**

652 **pore plate (white arrows in b and d). Scale bars = 2 μm.**

653

654
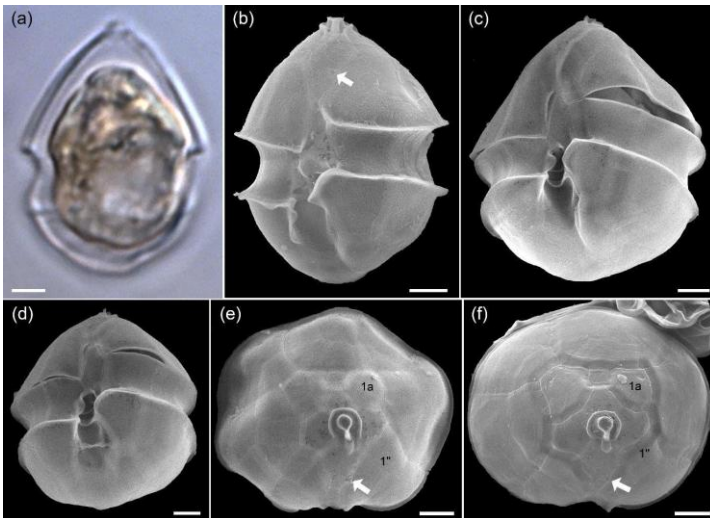
655 **Figure A03: LM (a) and SEM (b-f) of cells of the Amphidomatacean bloom stations identified as *Azadinium obesum*.**

656 **(b–d) Cells in ventral view. (e, f) Epitheca in apical view. Note the lack on an antapical spine, the position of the ventral**

657 **pore (white arrows in b, e, f) and the lack of contact between Plates 1a and 1" (kofoidian plate label notation) visible in**

658 **e) and f). Scale bars = 2 μm.**

659

660 **A 1.2. *Azadinium obesum***

661 Cells of the non-toxigeneic species *Az. obesum* were identified in the SEM samples based on the combination of the following

662 features: (1) no antapical spine, (2) ventral pore on the right side of Plate 1', and (3) no contact between Plates 1a and 1" (Fig.

663 A03). All such cells had a distinctly broad oval shape and were relatively large. In the light microscope, all relatively large

664 oval Amphidomataceae cells with a rounded hypotheca and no visible spine were therefore categorized as *Azadinium obesum*.

665
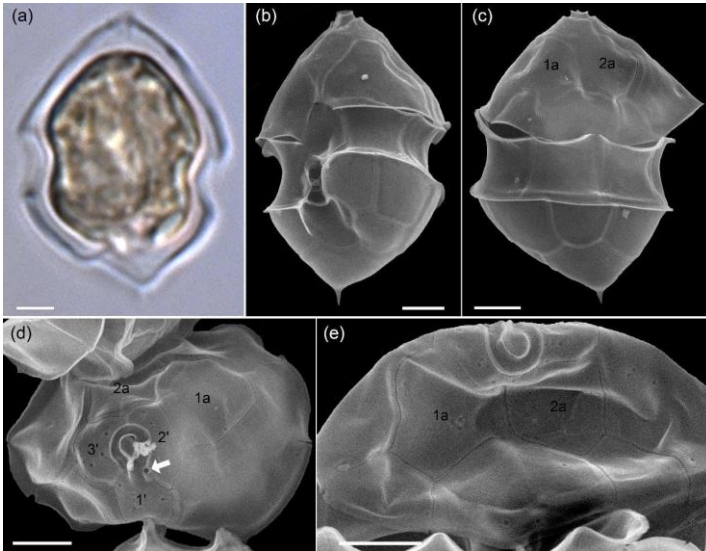
666
667 **Figure A04: LM (a) and SEM (b-f) of cells of the ~~Aa~~mphidomatacean bloom stations identified as** *Azadinium dalianense*.
668 **(b) Cell in ventral view. (c) Cell in dorsal view. (d) Epitheca in apical view. (f) Epitheca in dorsal view. Note the distinct**
669 **apical spine on a triangular bumpy hypotheca (a–c), the position of the ventral pore on the left side of the pore plate**
670 **(white arrow in d), the presence of only two large anterior intercalary plates 1a and 2a (c–e) and presence of only 3**
671 **apical plates in (d) (kofoidian plate label notation). Scale bars = 2 µm.**
672

673 **A 1.3.** *Azadinium dalianense*
674 With the rounded hypotheca, cells of *Az. obe*sum and *Az. spinosum* ribotype C were clearly distinguishable in the light
675 microscope from cells with a distinctly protruding bump, at the tip of which a small spine was present (Fig. A04a).
676 Corresponding cells detected in SEM preparations (Fig A04b–e) were identified as *Az. dalianense*, based on the combination
677 of the following features: (1) ventral pore on the left side of the pore plate, (2) asymmetrical hypotheca with a bump and a
678 distinct antapical spine, and (3) presence of only 3 apical plates and 2 anterior intercalary plates. Since all three features were
679 only rarely visible simultaneously due to the cell's orientation, the presence of the somewhat similar species *Az. perfusorium*
680 cannot be ruled out. *Az. perfusorium* also has a posterior small bump with a spine and a ventral pore located on the left side of
681 the pore plate, but it possesses 4 apical plates and 3 intercalary plates (Salas et al., 2021). However, neither the SEM nor
682 metabarcoding provided any indication of its presence in the samples. The occurrence of *Az. dalianense* in the region is well
683 documented by a series of strains isolated from the Argentine shelf in 2015 (Tillmann et al., 2019), and *Az. dalianense* was
684 also identified as part of *Azadinium* blooms in 1991(Tillmann and Akselman, 2016). Metabracoding additionally indicated the
685 presence of two differen ribotypes of *Az. dalianense*, namely E and B as defined in Tillmann et al. (2019), where all previous
686 strains from Argentina belong to the ribotype E clade. Accordingly, the majority of reads from the bloom station *Az. dalianense*
687 were from ribotype E (represented by strains H-4-E8 and N-12-04 in the reference dataset), whereas reads of ribotybe B
688 (represented by strain IFR-ADA-01C) made only ca. 0.02 % of all *Az. dalianense* reads. All strains of *Az. dalianese*
689 representing different ribotypes collected from various regions analysed so far were non-toxigenic.
690

691
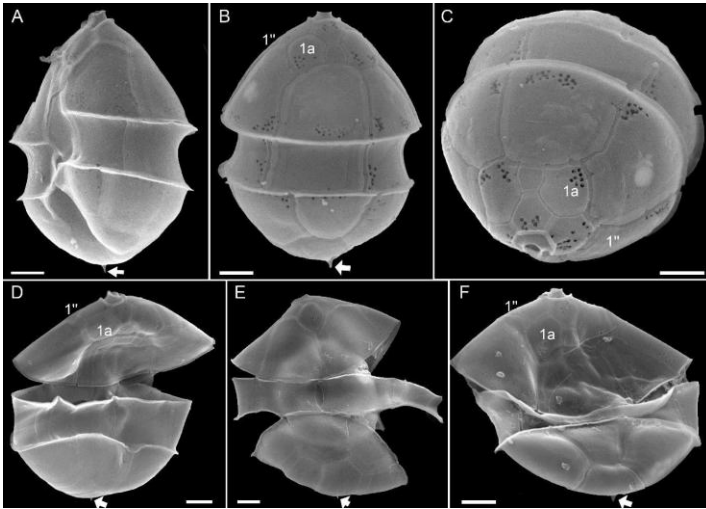
692 **Figure A05: SEM of yet unidentified cells of *Azadinium* sp. 1 of the Amphidomatacean bloom stations.** **(a) Cell in left-**
693 **lateral ventral view. (b) Cell in dorsal view. (c) Cell in apical view. (d–f) Cells in dorsal view. Note the small indistinct**
694 **apical spine (white arrow in a, b, d–f) and the lack of contact between plates 1a and 1'' (kofoidian plate label notation)**
695 **visible in b, c, d, f. Scale bars = 2 μm.**

696

697 The classification and quantification of *Az. obesum* and *Az. dalianense*, however, is complicated by the fact that a number of
698 cells of an unclear assignment were found in the samples (Fig. A05). These cells, like *Az. obesum*, (1) had a ventral pore on
699 the right side of Plate 1' and (2) no contact between Plates 1a and 1'', but unlike *Az. obesum*, they had a distinct, albeit small,
700 antapical spine. This combination of features is not known from any described *Azadinium* species, suggesting that this may be
701 a new species. However, for a complete description as a new *Azadinium* species, further investigations are necessary, ideally
702 adding sequence data and analyses of toxin production. In any case, it is clear that cells of this type will have been included in
703 the categories *Az. obesum* or *Az. spinosum* during the light microscope analyses and quantifications.

704
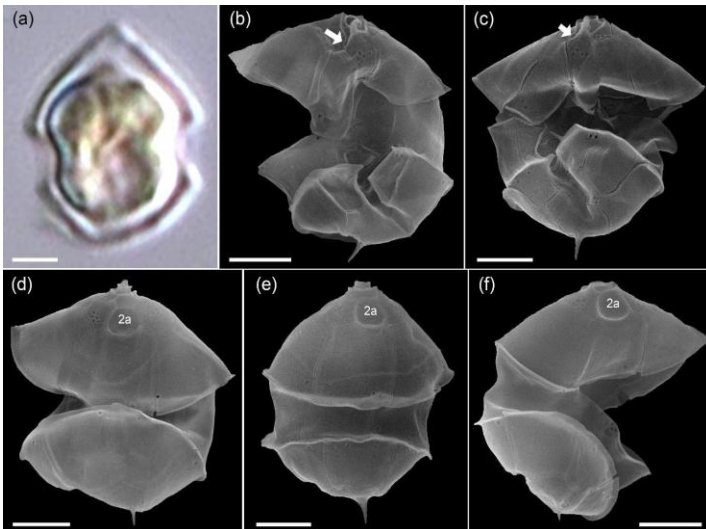
**Figure A06: LM (a) and SEM (b-f) of cells of the Amphidomatacean bloom stations identified as *Azadinium dexteroporum*. (b, c) Cells in ventral view. (d–f) Cells in dorsal view. Note the small size, the distinct antapical spine, the position of the ventral pore on the right side of the pore plate (white arrows in b, c,), and the concave central intercalary plate 2a visible in d–f. Scale bars = 2 μm.**

**A 1.4. Smaller Amphidomatacean species: *Azadinium dexteroporum*, *Amphidoma parvula*, and *Amphidoma languida***

While *Az. spinosum*, *Az. obesum*, and *Az. dalianense* fall into a slightly larger size class, a number of smaller *Azadinium* species were identified and categorized in the samples. One of them was *Az. dexteroporum* (Fig. A06), which was identified in the SEM by the following combination of features: (1) relatively small size, (2) presence of a distinct antapical spine, (3) a slightly posteriorly positioned ventral pore on the right side of the ventral plate, and (4) a distinctly concave central intercalary Plate 2a. Metabarcoding revealed a number reads for an *Azadinium* sp. 1 with *Az. dexteroporum* as closest species suggestion (line 7 in Table S01), however only with rather low similarity (90-95%) compared to the reference database. Global wise, there are only three available strains of *Az. dexteroporum*, and of those only one strain from the Mediterranean was identified as a producer of AZA (Rossi et al. 2017). In contrast, two additional strains from the North Atlantic, which also had marked sequence differences compared to the Mediterranean strain, did not produce AZAs (Tillmann et al. 2020). The low similarity of *Az. dexteroprum* reads from the present bloom samples thus indicate that the local population may represent a new ribotype quite distinct from the AZA-producing ribotype, and strain isolation of local *Az. dexteroporum* is needed to clarify its identity and toxin production potential.
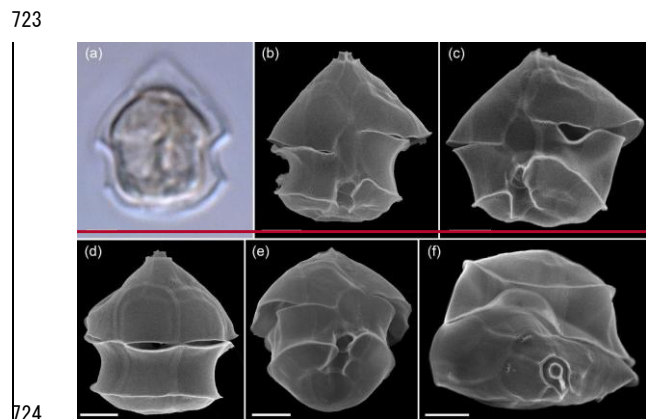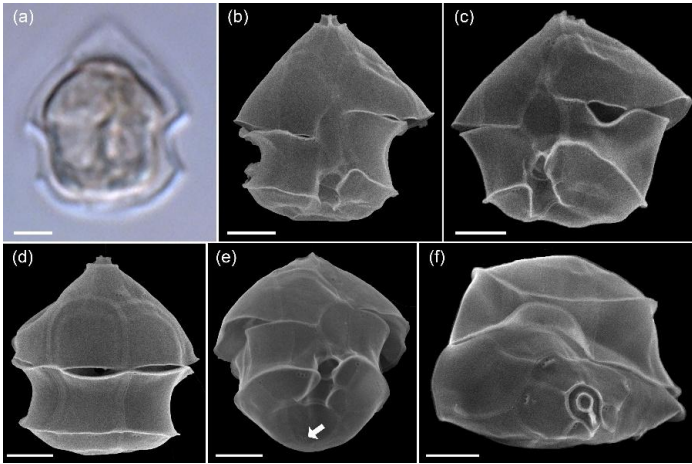
**Figure A07**: LM (a) and SEM (b-f) of cells of the Amphidomatacean bloom stations identified as *Amphidoma parvula*. **(b, c) Cells in ventral view. (d) Cell in dorsal view. (e) Cell in ventral antapical view. (f) cell in apical view. Note the small size, the flat hypotheca, the shape of the 1' plate visible in a, b, the group of pores in the second antapical plate (white arrow in e), and the relatively long apical plates visible in d and f. Scale bars = 2 μm.**

In the same size class, cells were also observed that were identified in SEM as *Amphidoma parvula* (Fig. A07) by (1) their flat hypotheca and (2) a characteristically shaped 1' plate. This non-toxigenic species was described in 2018 based on a culture isolated from the Argentine shelf (Tillmann et al., 2018). In accordance, a low number of reads with high similarity to *Am. parvula* strain H-1E9 (>98 %) recorded by metabarcoding. With its relatively long apical plates, *Am. parvula* could also be easily distinguished in the SEM from the similarly small *Am. languida*, which was also identified in SEM (Fig. A08). In *Am. languida*, (1) the small apical plates, and (2) the presence of a large characteristic antapical pore is a distinguishing feature.

737
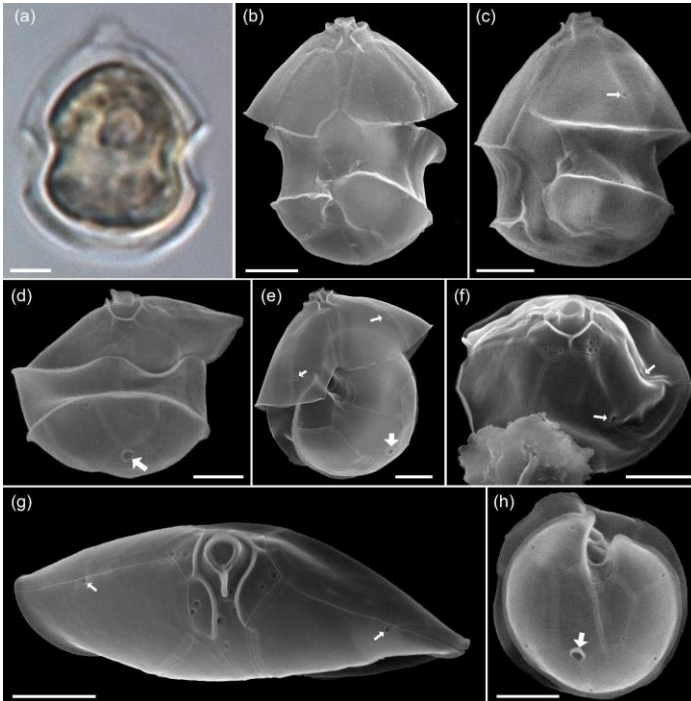
738 **Figure A08: LM (a) and SEM (b-f) of cells of the Amphidomatacean bloom stations identified as *Amphidoma languida*.**

739 **(b, c) Cells in ventral view. (d) Cell in dorsal view. (e) Cell with epitheca in ventral view and hypotheca in antapical**

740 **view. (f) Epitheca in lateral apical view. (g) epitheca in apical view. (h) Hypotheca in antapical view. Note the shape of**

741 **the 1' Plate visible in a), the distinct antapical pore in the second antapical plate (white arrows in d, e, h), and the**

742 **relatively short antapical plates visible in d, f, g. Also note that there are only single pores on precingular plates (small**

743 **white arrows in c, e, f, g). Scale bars = 2 µm.**

744

745 However, in 2024, a new species of *Amphidoma*, *Am. fulgens*, was described, which is morphologically almost identical to

746 *Am. languida* but shows significantly different sequence data and, different to *Am. languida*, does not produce azaspiracids

747 (Kuwata et al., 2024). *Amphidoma fulgens* was found to be widely distributed in the Pacific, but there are no records yet from

748 the Atlantic Ocean. Despite its presence in the bloom samples, there were no reads related with higher similarities to *Am.*

749 *languida* in the ITS metabarcoding data set, but only very few ready with rather low similarity to *Amphidoma entries in the*

750 *database-* This seem to be in line with the general notion that ITS sequencing of cultured strains of *Am. languida* in many

751 cases failed (Wietkamp et al. 2019). In fact, data of a previous metabarcoding study (Liu et al. 2023) showed that *Am. languida*

752 hits were abundant in Chinese waters in the LSU dataset but absent in the ITS-1 data set. While *Am. languida* and also *Am.*

753 *fulgens*, according to their original descriptions, only have one small pore on each precingulate plate (Tillmann et al., 2012;

754 Kuwata et al., 2024), there were also several cells of *Amphidoma* with three or more small pores on individual precingular

755 plates (Fig. A09a–d). To what extent these cells represent *Am. languida* or other yet undescribed and closely related species,

756 requires further clarification.

757
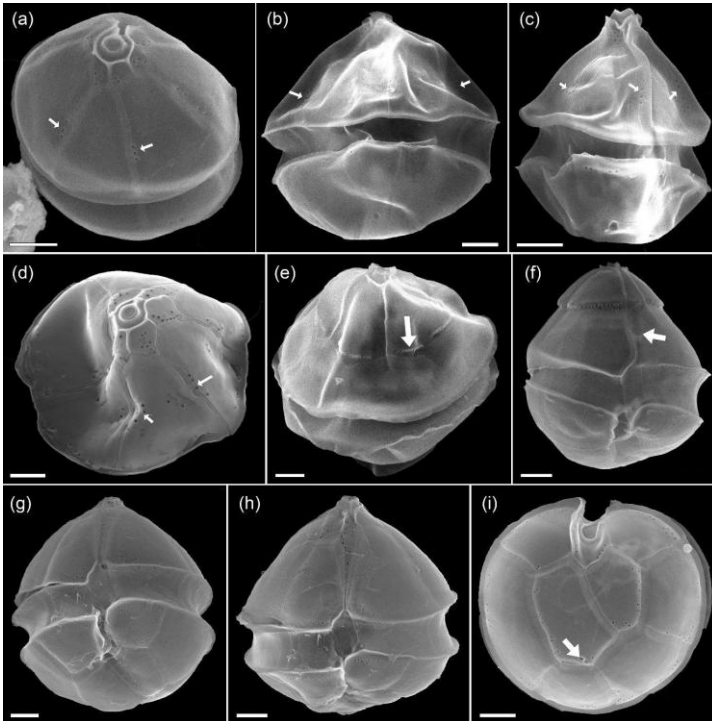
**Figure A09: SEM of unidentified cells of *Amphidoma* spp. of the Amphidomatacean bloom stations. (a–d) Cells in apical (a, c) or dorsal (b, c) view resembling *Amphidoma languida*, but with multiple pores in precingular plates (small white arrows in a–d). (e) A cell of *Amphidoma* sp. in dorsal view. Note the very long apical plates. The row of pores with a distinct rim on the apical plates (white arrow in e) resemble *Amphidoma alata*. (f) Cell of an unidentified *Amphidoma* sp. 1 in ventral view. Note the long apical plates, the ventral depression (white arrow in f), and the row of pore on the posterior suture of apical plates. (g, h). Two cells of *Amphidoma* sp. resembling *Amphidoma trioculata*. (i) Hypotheca in antapical view of an unidentified *Amphidoma*. Note the multiple pores on the plates and the presence of a very small antapical pores on the second antapical plate (white arrow in i). Scale bars = 2 μm.**

Due to the very similar size of *Az. dexteroporum*, *Am. parvula*, and *Am. languida*, all three species as identified with SEM are present in the one category of small amphidomatcean cells used for light microscopic analysis and quantification.

**A 1.5. Other Amphidomataceae**

In the SEM, a few other cells were observed, which can also be assigned to the genus *Amphidoma*. The epitheca found in dorsal view in Fig. A09e with its characteristic pore ridges on the large apical plates corresponds to *Am. alata*, a species which was described from the Argentina shelf (Tillmann, 2018). The cell depicted in Fig. A09f in ventral view likely represents a new species of *Amphidoma*. The cells in Figs. A09g-i likely correspond to *Am. trioculata*, another species described from Argentina (Tillmann, 2018), though assigning the isolated hypotheca (Fig. A09i) is difficult.

778
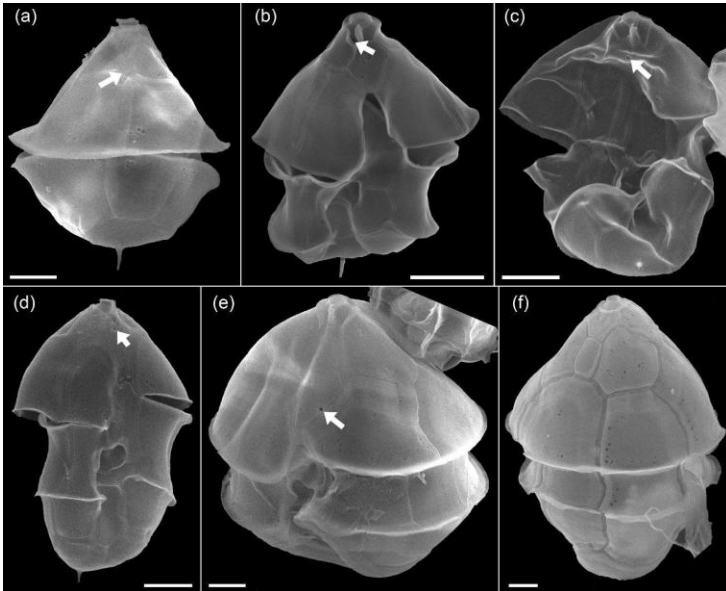
779 **Figure A10: SEM of unidentified cells of *Azadinium* spp. of the Amphidomatacean bloom stations. (a) Cell in dorsal**

780 **view. Note the very small and 5-sided intercalary plate (white arrow in a). (b) Cell of *Azadinium* sp. 1 in ventral view.**

781 **Note the very short 1' Plate and the position of the ventral pore inside the pore plate (white arrow in b). It may be**

782 **assumed but is not clear if (a) is the dorsal view of such an *Azadinium* sp. 1. (c. d), Two cells in ventral view of *Azadinium***

783 **sp. 2. Note the position of the ventral pore in apical position inside of Plate 1' (white arrows in c, d). (e) Cell of *Azadinium***

784 **sp. 3 in lateral ventral view. Note the position of the ventral pore (white arrow in e) and the rather long apical plates.**

785 **(f). Dorsal view of an *Azadinium* sp. 4 resembling in size and shape *Azadinium asperum*. Scale bars = 2 μm.**

786

787 Moreover, for a more complete description of the diversity of Amphidomataceae in the bloom sample, the following individual

788 findings (Fig. A10) should also be mentioned: A cell in dorsal view (Fig. A10a) had a very distinct antapical spine, relatively

789 large apical plates, and a small six-sided central intercalary plate. This combination of features has not been described in any

790 known *Azadinium* species, suggesting that this may represent a new species. The cell depicted in Fig. A10b had a distinct

791 antapical spine, a ventral pore on the right side of the pore plate, and a very short first apical plate, with the anterior sulcal

792 plate extending far into the epitheca. Both cells in Figs. A10b and c resemble *Az. spinosum* but differ in that the ventral pore

793 is centrally located within Plate 1' in the apical area. They likely correspond to the cells designated as *Azadinium* sp. 3 in Fig.

794 14 b, c, in Tillmann (2018). The cell in Fig. A10e had a ventral pore on the right side of Plate 1' (like *Az. spinosum* and *Az.*

795 *obesum*), but here the lateral apical plates were significantly larger than in these species. The cell in Fig. A10f in dorsal view

796 in terms of size and shape might correspond to *Az. asperum* described from the Argentine shelf (Tillmann, 2018), undoubtedly

797 an *Azadinium* species due to the apical pore and intercalary plates, does not match any previously described species based on

798 size (ca 20 μm cell length) and shape. This, along with the other cells in Fig. A09 which likely represents previously

799 undescribed species due to the unique combination of features, highlights the great diversity of Amphidomataceae in this 2021

800 bloom sample.

801

802 **Appendix B**

803

**Species diversity based on ITS1-based metabarcoding**

**Table B01: Species detected by Amplicon Sequence Variant (ASV) reads at stations GA01 and AA09.**

| Nr | species | Genbank | Identity % | GA01 | AA09 |
|---|---|---|---|---|---|
| 1 | *Amphidoma parvula* | KY996792 | **>98** | 19 | 0 |
| 2 | *Amphidoma* sp. 1 | OQ360107 | 90-95 | 158 | 200 |
| 3 | *Amphidoma* sp. 2 | LC788745 | 90-95 | 16 | 0 |
| 5 | *Azadinium dalianese* ribotype E | LS974150 | 90-95 | 41 | 63 |
|  |  |  | 95-98 | 33 | 58 |
|  |  |  | **>98** | 93.775 | 98.503 |
| 6 | *Azadinium dalianense* ribotype B | MF033117 | 95-98 | 9 | 0 |
|  |  |  | **>98** | 0 | 19 |
| 7 | *Azadinium* sp. 1 | OQ360091 | 90-95 | 36 | 41 |
| 8 | *Azadinium* sp. 2 | OQ360094 | **>98** | 6 | 5 |
| 9 | *Azadinium spinosum* ribotype C | MK405512 | **>98** | 17.006 | 7.589 |
| 10 | *Azadinium spinosum* ribotype B | LS974169 | **>98** | 0 | 37 |
| 11 | *Ansanella* sp. | MN604385 | 90-95 | 4 | 13 |
| 12 | *Bicheleria* sp. | KC895487 | 90-95 | 12 | 52 |
| 13 | *Bicheleria cincta* | KC895487 | **>98** | 6 | 17 |
| 14 | *Blastodinium oviforme* | JX473680 | 95-98 | 2 | 0 |
| 15 | *Karlodinium decipiens* | LC521288 | 95-98 | 0 | 7 |
|  |  |  | **>98** | 885 | 106 |
| 16 | *Karlodinium digitatum* | MN133932 | **>98** | 3 | 0 |
| 17 | *Kirithra asteri* | MW267275 | **>98** | 41 | 186 |
| 18 | *Pelagodinium beii* | KP843723 | **>98** | 48 | 77 |

Note: A total of 849 ASVs were identified; however, only 118 of these were successfully annotated at the species level (with over 97% similarity). This limitation may be attributed to the inadequacy of the ITS region database used in our study, which may have affected the taxonomic resolution of certain sequences.
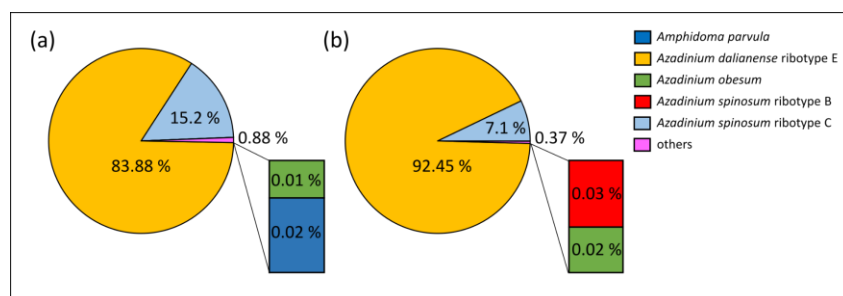
**Figure B01: Relative abundance (in %) of the Amphidomataceae species detected with metabarcoding targeting ITS1 regions at stations GA01 (a) and AA09 (b).**

**Appendix C**

**Overall appearance of the pure Amphidomataceae bloom in fixed field samples**
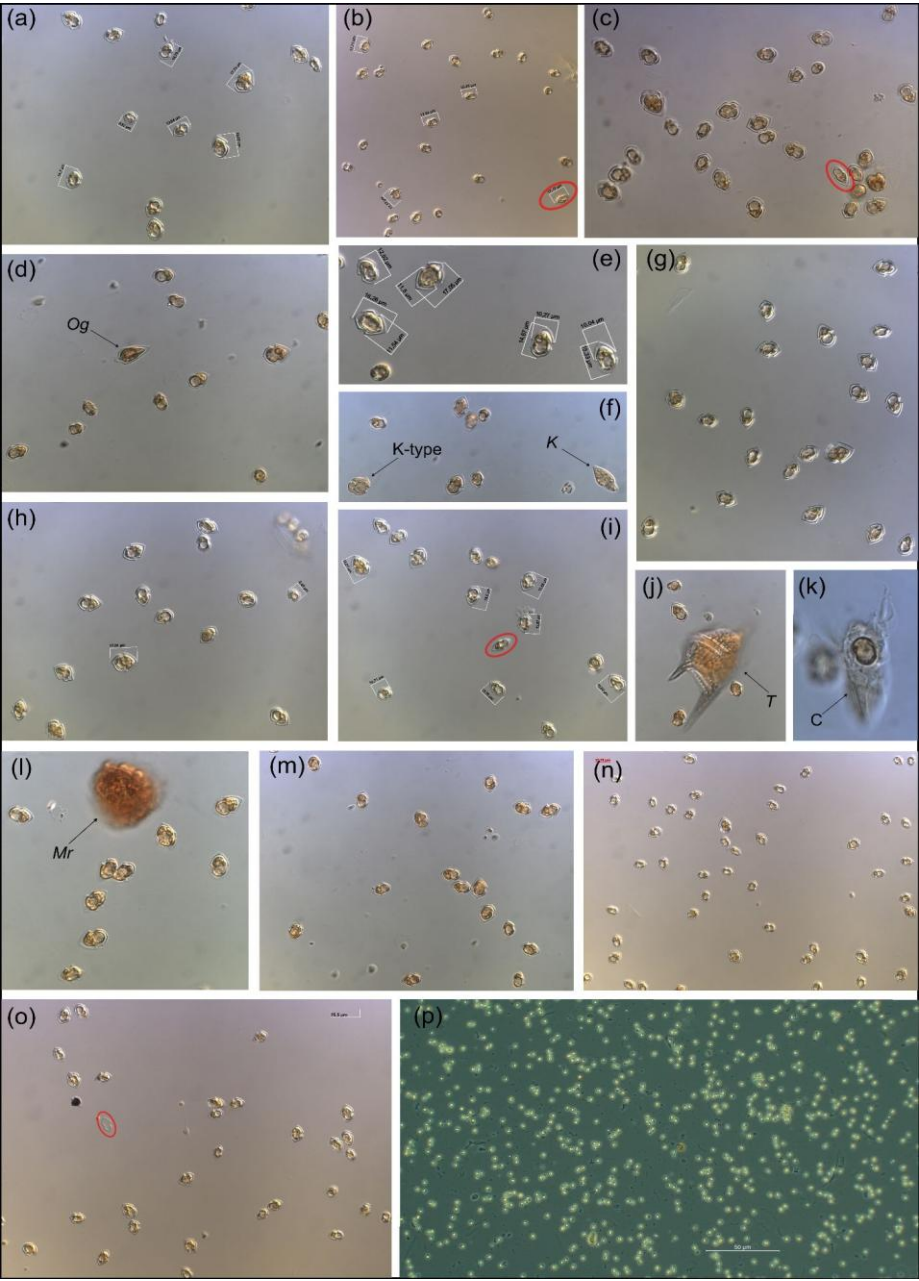
**Fig. C01: Micrographs of the Amphidomataceae bloom taken under light microscopy at low magnification: 200x. Only (e) was taken under 400x and (p) was taken using fluorescence in 100x. The toxic species *Azadinium spinosum* ribotype**

822 **B is indicated in a red circle. The arrows indicate other protists:** *Og*: *Oxytoxum gracile*, **K-type: Kareniacea-type cell,**

823 *K*: *Katodinium* **sp.,** *T*: *Tripos* **sp., C: ciliate with a cell of Amphidomataceae inside,** *Mr*: *Mesodinium rubrum*.

824

825 **Appendix D**

826

827 **Retention of particles in the blooming area**

828
829
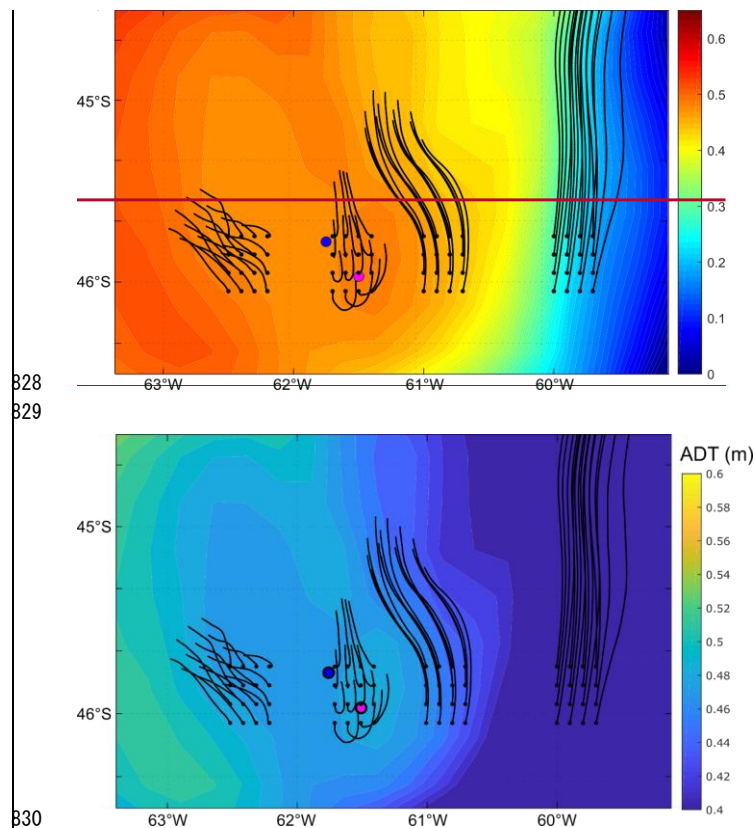
831 **Fig. D01: Background colours: Absolute Dynamic Topography (m) averaged from November 16 to 25. Black lines**

832 **correspond to the advection of particles for the same period after release at the points indicated with a black dot on**

833 **November 16.**

834

835 **Supplementary material:** Video showing the daily evolution from November 10 to 25, 2021 of the Finite-size Lyapunov

836 Exponent (FSLE) ridges in the area of the two locations with the Amphidomataceae bloom:  GA01, pink dot, sampled on

837 November 16, and AA09, blue dot, sampled on November 25. The two stations remained within the same water mass separated

838 by two maxima FSLE.

839

840 **Data availability:** The CTD data and the abundance of protistan species counted under light microscopy at the sampling

841 station GA01 and AA09, will be publicly available in the repository Pangaea Data Publisher (www.pangaea.de). Data from

842 the Gayoso cruise is available at: https://doi.pangaea.de/10.1594/PANGAEA.971564. Sequences obtained in this study are

843 available in the National Center for Biotechnology Information, Sequence Read Archive (http://www.ebi.ac.uk/ena).

844

845 **Author Contribution:** VAG conceptualised and designed the study, coordinated the planning and execution of field and
846 laboratory work, and secured funding. VAG and UT analysed the plankton samples using LM and SEM. MR processed the
847 satellite-derived chlorophyll data and the Lyapunov coefficients. CF and FR conducted field research and processed the CTD
848 data. VAG and BK processed the toxin samples. HG processed the DNA samples. MS analysed the geostrophic currents and
849 performed the particle tracking modelling. All co-authors contributed to the interpretation of the results. VAG prepared the
850 manuscript with contributions from all co-authors.

851

852 **Competing interests:** The authors declare that they have no conflict of interest.

853

854 **Acknowledgments and Funding:** VAG and MS acknowledge the BioMMAr consortium and the common grant received
855 from the Argentinean Initiative Pampa Azul (PIDT A6) to carry out the Gayoso cruise. VAG acknowledges the academic
856 mobility projects: FitoxNorPat, CONICET-DAAD call-2020, and Coastcarb, EUH2020-Marie Skłodowska-Curie grant
857 agreement N° 872690. VAG especially thanks Marcelo Acha from INIDEP, Argentina, for his invitation to participate in the
858 WG of the Marine Priority Area of Agujero Azul, from the Pampa Azul Initiative. VAG also thanks Annegret Mueller and
859 Thomas Max for their help and guidance in the laboratory work on processing toxin samples, VAG, UT and HG thanks
860 Annegret Müller for DNA extraction. The authors thank the Argentinean authorities, the captain and crew of the RV
861 Bernardo Houssay (Prefectura Naval Argentina) and the RV Victor Angelescu (INIDEP).

862

863 **References**

864

865 Abraham, E. R., Law, C. S., Boyd, P. W., Lavender, S. J., Maldonado, M. T., and Bowie, A. R. Importance of stirring in the
866 development of an iron-fertilized phytoplankton bloom. Nature, 407(6805), 727-730, https://doi.org/10.1038/35037555, 2000.
867 Akselman, R., and Negri, R.M. Blooms of *Azadinium* cf. *spinosum* Elbrächter et Tillmann (Dinophyceae) in northern shelf
868 waters of Argentina, Southwestern Atlantic. Harmful Algae 19, 30–38,https://doi.org/10.1016/j.hal.2012.05.004, 2012.
869 Akselman, R., Krock, B., Alpermann, T.J., Tillmann, U., Borel, C.M., Almandoz, G.O., and Ferrario, M.E. *Protoceratium*
870 *reticulatum* (Dinophyceae) in the austral Southwestern Atlantic and the first report on YTX-production in shelf waters of
871 Argentina. Harmful Algae 45, 40–52, https://doi.org/10.1016/j.hal.2015.03.001, 2015.
872 Alemany, D., Zavatteri, A., Prandoni, N., Giussi, A. R. Chapter 7: Fisheries in the Patagonian shelf break Front. In: The
873 Patagonian shelf-break Front. Ecology, Fisheries, Wildlife Conservation. Acha, M., Iribarne, O., Piola, A. (Eds). Springer
874 Nature. ISBN: 978-3-031-71189-3, doi.org/10.1007/978-3-031-71190-9_7, 2024.
875 Almandoz, G.O., Cefarelli, A.O., Diodato, S., Montoya, N.G., Benavides, Carignan, M., Hernando, M., Fabro, E., Metfies, K.,
876 Lundholm, N., Schloss, I.R., Alvarez, M., and Ferrario, M.E. Harmful phytoplankton in the Beagle Channel (South America)
877 as a potential threat to aquaculture activities. Mar. Poll. Bull. 145, 105–117, https://doi.org/10.1016/j.marpolbul.2019.05.026,
878 2019.
879 Anderson, C. R., Moore, S. K., Tomlinson, M. C., Silke, J., and Cusack, C. K. Living with harmful algal blooms in a changing
880 world: strategies for modelling and mitigating their effects in coastal marine ecosystems. In: Coastal and marine hazards,
881 risks, and disasters. Elsevier, ISBN: 978-0-12-396483-0, 495–561, 2015.

882 Anderson, D. M., Fensin, E., Gobler, C. J., Hoeglund, A. E., Hubbard, K. A., Kulis, D .M., Landsberg, J. H., Lefebvre, K. A.,
883 Provoost, P., Richlen, M. L., Smith, J. L., Solow, A. R., Trainer, V .L., Marine harmful algal blooms (HABs) in the United
884 States: history, current status and future trends. Harmful Algae 102, 101975, https://doi.org/10.1016/j.hal.2021.101975, 2021.
885 Balch, W. M., Drapeau, D. T., Bowler, B. C., Lyczkowski, E. R., Lubelczyk, L. C., Painter, S. C., Poulton, A. J. Surface
886 biological, chemical, and optical properties of the Patagonian Shelf coccolithophore bloom, the brightest waters of the Great
887 Calcite Belt. Limnol. Oceanogr. 59(5): 1715-1732, https://doi.org/10.4319/lo.2014.59.5.1715, 2014.
888 Becker, F., Romero, S. I., and Pisoni, J. P. Detection and characterization of submesoscale eddies from optical images: a case
889 study in the Argentine continental shelf. Int. J. Remote Sens., 44(10), 3146-3159,
890 https://doi.org/10.1080/01431161.2023.2216853, 2023.
891 Beron-Vera, F.J., Bodnariuk, N., Saraceno, M., Olascoaga, M.J., Simionato, C. Stability of the Malvinas current. Chaos 30
892 (1), 13152. https://doi.org/10.1063/, 2020.
893 Cadaillon, A. M., Mattera, B., Albizzi, A., Montoya, N., Maldonado, S., Rey, A. R., Riccialdelli, L., Almandoz, G.O. and
894 Schloss, I. R. Multispecies mass mortality in the Beagle Channel associated with paralytic shellfish toxins. Harmful Algae,
895 132, 102581, https://doi.org/10.1016/j.hal.2024.102581, 2024.
896 Carreto, J. I., Montoya, N. G., Carignan, M. O., Akselman, R., Acha, E. M., and Derisio, C. Environmental and biological
897 factors controlling the spring phytoplankton bloom at the Patagonian shelf break front–Degraded fucoxanthin pigments and
898 the importance of microzooplankton grazing. Prog.  Oceanogr., 146, 1-21, https://doi.org/10.1016/j.pocean.2016.05.002,
899 2016.
900 Combes, V. and Matano, R. P. The Patagonian shelf circulation: Drivers and variability. Prog Oceanogr. 167: 24-43,
901 https://doi.org/10.1016/j.pocean.2018.07.003, 2018.
902 Corredor-Acosta, A., Galán, A., Saldías, G. S., Mardones, J. I., Medellín-Mora, J., Frangopulos, M., Shiozaki T., Harada,
903 N., González H. E., and Iriarte, J. L. Oceanic phytoplankton structure off western Patagonia during the austral summer:
904 Implications for harmful algal blooms. Prog. Oceanogr., 231, 103409, 2025.
905 D'Agostino, V.C., Krock, B., Degrati, M., Sastre, V., Santinelli, N., Krohn, T. and Hoffmeyer, M. S. Occurrence of toxigenic
906 microalgal species and phycotoxin accumulation in mesozooplankton in northern Patagonian gulfs, Argentina. Environ.
907 Toxicol. Chem. 38(10), 2209-2223,https://doi.org/10.1002/etc.4538, 2019.
908 Delgado, A. L., Hernández-Carrasco, I., Combes, V., Font-Muñoz, J., Pratolongo, P. D., and Basterretxea, G. Patterns and
909 trends in chlorophyll-*a* concentration and phytoplankton phenology in the biogeographical regions of Southwestern Atlantic.
910 J. Geophys. Res.: Oceans, 128(9), e2023JC019865,https://doi.org/10.1029/2023JC019865,  2023.
911 Della Penna, A., De Monte, S., Kestenare, E., Guinet, C., and  d'Ovidio, F. Quasi-planktonic behavior of foraging top marine
912 predators. Scientific Reports, 5(1), 18063, https://doi.org/10.1038/srep18063, 2015.
913 d'Ovidio, F., Fernández, V., Hernández-García, E. and  López, C. Mixing structures in the mediterranean sea from finite-size
914 lyapunov exponents. Geophys. Res. Lett. 31, 17203, https://doi.org/10.1029/2004GL020328, 2004.
915  d'Ovidio, F., Isern-Fontanet, J., López, C., Hernández-García, E. and García-Ladona, E. Comparison between Eulerian
916 diagnostics and finite-size Lyapunov exponents computed from altimetry in the Algerian basin. Deep-Sea Res. I 56, 15–
917 31,https://doi.org/10.1016/j.dsr.2008.07.014, 2009.
918 Fabro, E., Almandoz, G. O., Krock, B., and Tillmann, U. Field observations of the dinoflagellate genus *Azadinium* and
919 azaspiracid toxins in the south-west Atlantic Ocean. Mar. Freshw. Res. 71 (7), 832–843, https://doi.org/10.1071/MF19124,
920 2019.
921 Ferronato C., Berden G., Rivarossa M. and Guinder V.A. Wind-driven currents and water masses shape spring phytoplankton
922 distribution and composition in hydrologically complex, productive shelf waters. Limnol. Oceanogr.,
923 https://doi.org/10.1002/lno.12413, 2023.
924 Ferronato, C., Guinder, V.A., Rivarossa, M., Saraceno, M., Ibarbalz, F., Tillmann, U., Almandoz, G., Bourdin, G.,

925  D'Agostino, V., Gilabert, A., Loizaga, R., López Abbate, C., Nocera, A. C., Silva, R., and Flombaum, P. Insights into
926  protistan plankton blooms in the highly dynamic Patagonian shelf and adjacent ocean basin in the Southwestern Atlantic. J.
927  Geophys. Res.: Oceans, https://doi.org/10.1029/2024JC021412, 2025.

928  Frey, D. I., Piola, A. R., and Morozov, E. G. Convergence of the Malvinas current branches near 44° S. Deep Sea Research
929  Part I: Oceanogr. Res. Papers, 104023. https://doi.org/10.1016/j.dsr.2023.104023, 2023.

930  García, V. M. T., Garcia, C. A. E., Mata, M. M., Pollery, R. C., Piola, A. R., Signorini, S. R., McClain, C. R., and Iglesias-
931  Rodriguez, M. D. Environmental factors controlling the phytoplankton blooms at the Patagonia shelf break in spring. Deep-
932  Sea Res. I: Oceanogr Res. Pap. 55(9): 1150-1166, https://doi.org/10.1016/j.dsr.2008.04.011, 2008.

933  GEBCO  Compilation  Group,  General  Bathymetric  Chart  of  the  Ocean.  GEBCO  2021  grid.
934  https://www.gebco.net/data_and_products/historical_data_sets/#gebco_2021, 2021.

935  Genitsaris, S., Stefanidou, N., Sommer, U. and Moustaka-Gouni, M. Phytoplankton blooms, red tides and mucilaginous
936  aggregates in the urban Thessaloniki Bay, Eastern Mediterranean. Diversity, 11(8), 136, https://doi.org/10.3390/d11080136,
937  2019.

938  Giddings, S. N., MacCready, P., Hickey, B. M., Banas, N. S., Davis, K. A., Siedlecki, S. A., Trainer, V .L., Kudela, R. M.,
939  Pelland, N. A., and Connolly, T. P. Hindcasts of potential harmful algal bloom transport pathways on the Pacific Northwest
940  coast. J. Geophys. Res.: Oceans 119 (4), 2439–2461, https://doi.org/10.1002/2013JC009622, 2014.

941  Gilabert, A. S., López-Abbate, C., Flombaum, P., Unrein, F., Arbilla, L. A., Garzón-Cardona, J. E., Martinez, A. M., Ibarbalz,
942  F. M., Vincent, F., Saraceno M., Ruiz-Etcheverry, L. A., Ferronato, C., Guinder, V. A., Silva, R., Uibrig, R. A., D'Agostino,
943  V., Loizaga, R., and Lara, R. J. Planktonic drivers of carbon transformation during different stages of the spring bloom at the
944  Patagonian Shelf-break front, Southwestern Atlantic Ocean. Biogeochemistry 168 (1), 1-25, https://doi.org/10.1007/s10533-
945  024-01192-6, 2025.

946  Glibert, P. M. Margalef revisited: a new phytoplankton mandala incorporating twelve dimensions, including nutritional
947  physiology. Harmful Algae, 55, 25-30, https://doi.org/10.1016/j.hal.2016.01.008, 2016.

948  Guinder, V.A., Ferronato, C., Segura, V., Dogliotti, A., and Lutz, V. The phytoplankton of the Patagonian shelf break Front.
949  In: The Patagonian shelf-break Front. Ecology, Fisheries, Wildlife Conservation. Acha, M., Iribarne, O., Piola, A. (Eds).
950  Aquatic Ecology Series, 13. Springer, Cham.  https://doi.org/10.1007/978-3-031-71190-9_3, 2024.

951  Guinder V.A., Tillmann U., Krock B., Delgado A., Garzón-Cardona J.E., Katja M., López Abbate M.C., Silva R. and Lara
952  R. Plankton multiproxy analyses in the Northern Patagonian Shelf, Argentina: community structure, phycotoxins and
953  characterization of toxic *Alexandrium* strains. Front. Mar. Sci. 5: 394, https://doi.org/10.3389/fmars.2018.00394, 2018.

954  Guinder, V. A., Malits, A., Ferronato, C., Krock, B., Garzón-Cardona, J. E., and Martínez, A. Microbial plankton
955  configuration in the epipelagic realm from the Beagle Channel to the Burdwood Bank, a Marine Protected Area in Sub-
956  Antarctic waters. Plos One 15(5): e0233156, https://doi.org/10.1371/journal.pone.0233156, 2020.

957  Hallegraeff, G. M., Anderson, D. M., Belin, C., Bottein, M. Y. D., Bresnan, E., Chinain, M., Enevoldsen, H., Iwataki, M.,
958  Karlson, B., McKenzie, C.H., Sunesen, I., Pitcher, G. C., Provoost, P., Richardson, A., Schweibold, L., Tester, P. A., Trainer,
959  V. L., Yniguez, A. T., and Zingone, A. Perceived global increase in algal blooms is attributable to intensified monitoring and
960  emerging bloom impacts. Commun. Earth Environ. 2 (1), 1–10, https://doi.org/10.1038/s43247-021-00178-8, 2021.

961  Haller, G. and Beron-Vera, F. J. Geodesic theory of transport barriers in two-dimensional flows. Phys. D: Nonlinear Phenom.,
962  241(20), 1680-1702, https://doi.org/10.1016/j.physd.2012.06.012, 2012.

963  Hansen, H. P., Koroleff, F. Determination of nutrients. Methods of seawater analysis, (Grasshoff, K., Kremling, K. and
964  Ehrhardt, M. (Eds.). Verlag Chemie, 159-228, 1999.

965  Hasle, G., 1987. Concentrating phytoplankton. Settling. The inverted microscope method. In: Sournia, A. (Ed.). Monographs
966  on Oceanographic Methodology: Phytoplankton Manual. Unesco, Paris, pp. 88–96.

967  Hernández-Carrasco I., Alou-Font E., Dumont P. A., Cabornero A., Allen J., and Orfila A. Lagrangian flow effects on

968 phytoplankton abundance and composition along filament-like structures. Prog. Oceanogr., 189, 102469,
969 https://doi.org/10.1016/j.pocean.2020.102469, 2020.

970 Iriarte, J. L., Pizarro, G., and Frangopulos, M. Harmful algal blooms in Patagonian fjords and channels systems: Recent
971 advances, gaps, and priorities in a changing ocean. Prog. Oceanogr., 217, 103087,
972 https://doi.org/10.1016/j.pocean.2023.103087, 2023.

973 Jeffrey S. T. and Humphrey G. F. New spectrophotometric equations for determining chlorophylls $a$, $b$, $c_1$ and $c_2$ in higher
974 plants, algae and natural phytoplankton. Biochem. Physiol. Pflanzen, 167(2), 191-194, https://doi.org/10.1016/S0015-
975 3796(17)30778-3, 1975.

976 Kelley, D. E., Richards, C. and Layton, C. oce: An R package for oceanographic analysis. J. Open Source Softw. 7: 3594,
977 2022.

978 Krock, B., Tillmann, U., Tebben, J., Trefault, N., and Gu, H. Two novel azaspiracids from *Azadinium poporum*, and a
979 comprehensive compilation of azaspiracids produced by Amphidomataceae, (Dinophyceae). Harmful Algae 82, 1–8,
980 https://doi.org/10.1016/j.hal.2018.12.005, 2019.

981 Kuwata, K., Lum, W.M., Takahashi, K., Benico, G., Takahashi, K., Lim, P.T., Leaw, C.P., Uchida, H., Ozawa, M.,
982 Matsushima, R., Watanabe, R., Suzuki, T., and Iwataki, M. Phylogeny and ultrastructure of a non-toxigenic dinoflagellate
983 *Amphidoma fulgens* sp. nov. (Amphidomataceae, Dinophyceae), with a wide distribution across Asian Pacific. Harmful Algae
984 138, 102701, https://doi.org/10.1016/j.hal.2024.102701, 2024.

985 Lago, L. S., Saraceno, M., Piola, A. R., and Ruiz-Etcheverry, L. A. Volume transport variability on the northern argentine
986 continental shelf from in situ and satellite altimetry data. J. Geophys. Res.: Oceans, 126(2), e2020JC016813,
987 https://doi.org/10.1029/2020JC016813, 2021.

988 Lehahn, Y., d'Ovidio, F., Lévy, M., and Heifetz, E. Stirring of the northeast Atlantic spring bloom: A Lagrangian analysis
989 based on multisatellite data. *J. Geophys. Res.: Oceans*, *112*(C8), https://doi.org/10.1029/2006JC003927, 2007.

990 Lehahn, Y., Koren, I., Sharoni, S., d'Ovidio, F., Vardi, A. and Boss, E. Dispersion/dilution enhances phytoplankton blooms
991 in low-nutrient waters. Nat. Commun., 8(1), 14868, https://doi.org/10.1038/ncomms14868, 2017.

992 Lévy, M., Franks, P. J., and Smith, K. S. The role of submesoscale currents in structuring marine ecosystems. Nat. Commun.,
993 9(1), 4758, https://doi.org/10.1038/s41467-018-07059-3, 2018.

994 Lin S., Litaker R.W. and Sunda, W.G. Phosphorus physiological ecology and molecular mechanisms in marine phytoplankton.
995 J. Phycol., 52(1), 10-36, https://doi.org/10.1111/jpy.12365, 2016.

996 Liu M., Tillmann U., Ding G., Wang A. and Gu, H. Metabarcoding revealed a high diversity of Amphidomataceae
997 (Dinophyceae) and the seasonal distribution of their toxigenic species in the Taiwan Strait. Harmful Algae, 124, 102404.
998 https://doi.org/10.1016/j.hal.2023.102404, 2023.

999 Lopez-Rivera, A., O'callaghan, K., Moriarty, M., O'Driscoll, D., Hamilton, B., Lehane, M., James, K.J., Furey, A.. First
1000 evidence of azaspiracids (AZAs): a family of lipophilic polyether marine toxins in scallops (*Argopecten purpuratus*) and
1001 mussels (*Mytilus chilensis*) collected in two regions of Chile. Toxicon 55 (4), 692–701,
1002 https://doi.org/10.1016/j.toxicon.2009.10.020, 2010.

1003 Mahadevan, A. The impact of submesoscale physics on primary productivity of plankton. Annu. Rev. Mar. Sci., 8(1), 161-
1004 184, https://doi.org/10.1146/annurev-marine-010814-015912, 2016.

1005 Mangolte, I., Lévy, M., Haëck, C., and Ohman, M. D. Sub-frontal niches of plankton communities driven by transport and
1006 trophic interactions at ocean fronts. *Biogeosciences*, *20*(15), 3273-3299, https://doi.org/10.5194/bg-20-3273-2023, 2023.

1007 Maritorena, S., d'Andon, O. H. F., Mangin, A., and Siegel, D. A. Merged satellite ocean color data products using a bio-
1008 optical model: Characteristics, benefits and issues. Remote Sens. Environ., 114(8), 1791-1804,
1009 https://doi.org/10.1016/j.rse.2010.04.002, 2010.

1010 Martinetto, P., Alemany, D., Botto, F., Mastrángelo, M., Falabella, Acha, E.M., Antón, G., Bianchi, A., Campagna, C.,

Cañete, G., Filippo, P., Iribarne, O., Laterra, P., Martínez, P., Negri, R., Piola, A.R., Romero, S.I., Santos, D., and Saraceno, M. Linking the scientific knowledge on marine frontal systems with ecosystem services. Ambio 49 (2), 541–556, https://doi.org/10.1007/s13280-019-01222-w, 2019.

Matano, R. P., Palma, E. D., and Piola, A. R. The influence of the Brazil and Malvinas Currents on the Southwestern Atlantic Shelf circulation. Ocean Sci. 6(4): 983-995, https://doi.org/10.5194/os-6-983-2010, 2010.

McGirr, S., Clarke, D., Kilcoyne, Silke, J., and Touzet, N. Co-localisation of Azaspiracid Analogs with the Dinoflagellate Species *Azadinium spinosum* and *Amphidoma languida* in the Southwest of Ireland. Microb Ecol 83, 635–646, https://doi.org/10.1007/s00248-021-01777-w, 2022.

Palma, E. D., Matano, R. P., and Piola, A. R. A numerical study of the southwestern Atlantic shelf circulation: Stratified Ocean response to local and offshore forcing. J. Geophys. Res. https://doi.org/10.1029/2007jc004720, 2008.

Piola, A. R., Bodnariuk, N., Combes, V., Franco, B. C., Matano, R. P., Palma, E. D., Romero, S. I., Saraceno, M., Urricariet, M. M. Anatomy and dynamics of the Patagonia shelf break front. In: The Patagonian shelf-break Front. Ecology, Fisheries, Wildlife Conservation. Acha, M., Iribarne, O., Piola, A. (Eds). Springer Nature. ISBN: 978-3-031-71189-3, 2024.

Pitcher, G. C., Figueiras, F. G., Hickey, B. M., & Moita, M. T. The physical oceanography of upwelling systems and the development of harmful algal blooms. Prog. Oceanogr., 85(1-2), 5-32, https://doi.org/10.1016/j.pocean.2010.02.002, 2010.

Ramírez F.J., Guinder V.A., Ferronato C. and Krock B. Increase in records of toxic phytoplankton and associated toxins in water samples in the Patagonian Shelf (Argentina) over 40 years of field surveys. Harmful Algae, 118: 102317, https://doi.org/10.1016/j.hal.2022.102317, 2022.

Raine, R. A review of the biophysical interactions relevant to the promotion of HABs in stratified systems: the case study of Ireland. Deep Sea Res. Part II 101, 21–31, https://doi.org/10.1016/j.dsr2.2013.06.021, 2014.

Rossi, R., Dell'Aversano, C., Krock, B., Ciminiello, P., Percopo, I., Tillmann, U., Soprano, V., and Zingone, A. Mediterranean *Azadinium dexteroporum* (Dinophyceae) produces AZA-35 and six novel azaspiracids: a structural study by a multi-platform mass spectrometry approach. Anal. Bioanal. Chem. 409, 1121-1134, https://doi.org/10.1007/s00216-016-0037-4, 2017.

Salas R., Tillmann U., Gu H., Wietkamp S., Krock B. and Clarke D. Morphological and molecular characterization of multiple new *Azadinium* strains revealed a high diversity of non-toxigenic species of Amphidomataceae (Dinophyceae) including two new *Azadinium* species in Irish waters, North East Atlantic. Phycol. Res., 69(2), 88-115, https://doi.org/10.1111/pre.12448, 2021.

Salyuk P.A., Mosharov S.A., Frey D.I., Kasyan V.V., Ponomarev V.I., Kalinina O.Y., Morozov E.G., Latushkin A.A., Sapozhnikov P.V., Ostroumova S.A., Lipinskaya N.A., Budyansky M.V., Chukmasov P.V., Krechik V.A., Uleysky M.Y., Fayman P.A., Mayor A.Y., Mosharova I.V., Chernetsky A.D., Shkorba S.P. and Shved N. A. Physical and biological features of the waters in the outer Patagonian shelf and the Malvinas Current. Water, 14(23), 3879, https://doi.org/10.3390/w14233879, 2022.

Ser-Giacomi, E., Martinez-Garcia, R., Dutkiewicz, S., and Follows, M. J. A. Lagrangian model for drifting ecosystems reveals heterogeneity-driven enhancement of marine plankton blooms. Nat. Commun. 14(1), 6092, https://doi.org/10.1038/s41467-023-41469-2, 2023.

Smayda, T.J. Turbulence, watermass stratification and harmful algal blooms: an alternative view and frontal zones as "pelagic seed banks". Harmful Algae 1 (1), 95–112, https://doi.org/10.1016/S1568-9883(02)00010-0, 2002.

Sunesen, I., Méndez, S. M., Mancera-Pineda, J. E., Dechraoui-Bottein, M. Y., and Enevoldsen, H. The Latin America and Caribbean HAB status report based on OBIS and HAEDAT maps and databases. Harmful Algae 102, 101920, https://doi.org/10.1016/j.hal.2020.101920, 2021.

Tillmann, U., Salas, R., Gottschling, M., Krock, B., O´Driscoll, D., and Elbrächter, M. *Amphidoma languida* sp. nov. (Dinophyceae) reveals a close relationship between *Amphidoma* and *Azadinium*. Protist 163, 701-719, https://doi.org/10.1016/j.protis.2011.10.005, 2012.

1054    Tillmann, U., and Akselman, R. Revisiting the 1991 algal bloom in shelf waters off Argentina: *Azadinium luciferelloides* sp. nov. (Amphidomataceae, Dinophyceae) as the causative species in a diverse community of other amphidomataceans. Phycol. Res. 64, 160-175, https://doi.org/10.1111/pre.12133, 2016.

1057    Tillmann, U., Trefault, N., Krock, B., Parada-Pozo, G., De la Iglesia, R., and Vásquez, M. Identification of *Azadinium poporum* (Dinophyceae) in the Southeast Pacific: morphology, molecular phylogeny, and azaspiracid profile characterization. J. Plank. Res. 39 (2), 350–367, https://doi.org/10.1093/plankt/fbw099, 2017a.

1060    Tillmann, U., Sánchez-Ramírez, S., Krock, B., and Bernales-Jiménez, A.  A bloom of *Azadinium polongum* in coastal waters off Peru. Rev. Biol. Mar. Oceanogr, 52(3), 591-610, http://dx.doi.org/10.4067/S0718-19572017000300015, 2017b.

1062    Tillmann, U. Amphidomataceae. In: Shumway, S.E., Burkholder, J.M., Morton, S. L. (Eds.), Harmful Algal Blooms: A compendium Desk Reference. Wiley, Singapore, pp. 575–582, ISBN: 978-1-118-99467-2, 2018.

1064    Tillmann, U. Electron microscopy of a 1991 spring plankton sample from the Argentinean shelf reveals the presence of four new species of Amphidomataceae (Dinophyceae). Phycol. Res. 66, 269-290, https://doi.org/10.1111/pre.12225, 2018.

1066    Tillmann, U., Gottschling, M., Guinder, V. and Krock, B. *Amphidoma parvula* (Amphidomataceae), a new planktonic dinophyte from the Argentine Sea. Eur. J. Phycol. 53, 14-28, https://doi.org/10.1080/09670262.2017.1346205, 2018.

1068    Tillmann, U., Gottschling, M., Krock B., Smith, K.F. and Guinder, V.A. High abundance of Amphidomataceae (Dinophyceae) during the 2015 spring bloom of the Argentinean Shelf and a new, non-toxigenic ribotype of *Azadinium spinosum*. Harmful Algae, 84: 244-260, https://doi.org/10.1016/j.hal.2019.01.008, 2019.

1071    Tillmann, U., Wietkamp, S., Krock, B., Tillmann, A., Voss, D. and Gu, H. Amphidomataceae (Dinophyceae) in the western Greenland area, including the description of *Azadinium perforatum* sp. nov. Phycologia 59, 63-88, https://doi.org/10.1080/00318884.2019.1670013, 2020.

1074    Tillmann, U., Wietkamp, S., Gu, H., Krock, B., Salas, R. and Clarke, D. Multiple new strains of Amphidomataceae (Dinophyceae) from the North Atlantic revealed a high toxin profile variability of *Azadinium spinosum* and a new non-toxigenic *Az.* cf. *spinosum*. Microorganisms, 9(1), 134, https://doi.org/10.3390/microorganisms9010134, 2021.

1077    Turner, A.D. and Goya, A.B. Occurrence and profiles of lipophilic toxins in shellfish harvested from Argentina. Toxicon 102, 32–42, https://doi.org/10.1016/j.toxicon.2015.05.010, 2015.

1079    Wells, M. L., Karlson, B., Wulff, A., Kudela, R., Trick, C., Asnaghi, V., ... and Trainer, V. L. Future HAB science: Directions and challenges in a changing climate. Harmful algae, 91, 101632, https://doi.org/10.1016/j.hal.2019.101632, 2020.

1081    Wietkamp, S., Krock, B., Clarke, D., Voß, D., Salas, R., Kilcoyne, J., and Tillmann, U. Distribution and abundance of azaspiracid-producing dinophyte species and their toxins in North Atlantic and North Sea waters in summer 2018. PLoS One 15, e0235015, https://doi.org/10.1371/journal.pone.0235015, 2020.

1084    Wilson, C., Sastre, A. V., Hoffmeyer, M., Rowntree, V. J., Fire, S. E., Santinelli, N. H., Ovejero, S. D., D'Agostino, V., Marón, C. F., Doucette, G., J., Broadwater, M. H., Wang, Z., Montoya, N., Seger, J., Adler, F. R., Sironi, M. and Uhart M. M.,Southern right whale (*Eubalaena australis*) calf mortality at Península Valdés, Argentina: Are harmful algal blooms to blame? Mar. Mammal Sci. 32(2): 423-451, https://doi.org/10.1111/mms.12263, 2015.